



## DEFENSE TECHNICAL INFORMATION CENTER

*Information for the Defense Community*

DTIC<sup>®</sup> has determined on 

Month	Day	Year
02	02	2009

 that this Technical Document has the Distribution Statement checked below. The current distribution for this document can be found in the DTIC<sup>®</sup> Technical Report Database.

☒ **DISTRIBUTION STATEMENT A.** Approved for public release; distribution is unlimited.

☐ **© COPYRIGHTED.** U.S. Government or Federal Rights License. All other rights and uses except those permitted by copyright law are reserved by the copyright owner.

☐ **DISTRIBUTION STATEMENT B.** Distribution authorized to U.S. Government agencies only. Other requests for this document shall be referred to controlling office.

☐ **DISTRIBUTION STATEMENT C.** Distribution authorized to U.S. Government Agencies and their contractors. Other requests for this document shall be referred to controlling office.

☐ **DISTRIBUTION STATEMENT D.** Distribution authorized to the Department of Defense and U.S. DoD contractors only. Other requests shall be referred to controlling office.

☐ **DISTRIBUTION STATEMENT E.** Distribution authorized to DoD Components only. Other requests shall be referred to controlling office.

☐ **DISTRIBUTION STATEMENT F.** Further dissemination only as directed by controlling office or higher DoD authority.

*Distribution Statement F is also used when a document does not contain a distribution statement and no distribution statement can be determined.*

☐ **DISTRIBUTION STATEMENT X.** Distribution authorized to U.S. Government Agencies and private individuals or enterprises eligible to obtain export-controlled technical data in accordance with DoDD 5230.25.

**REPORT DOCUMENTATION PAGE***Form Approved*  
**OMB No. 0704-0188**

Public reporting burden for this collection of information is estimated to average 1 hour per response, including the time for reviewing instructions, searching data sources, gathering and maintaining the data needed, and completing and reviewing the collection of information. Send comments regarding this burden estimate or any other aspect of this collection of information, including suggestions for reducing this burden to Washington Headquarters Service, Directorate for Information Operations and Reports, 1215 Jefferson Davis Highway, Suite 1204, Arlington, VA 22202-4302, and to the Office of Management and Budget, Paperwork Reduction Project (0704-0188) Washington, DC 20503.

**PLEASE DO NOT RETURN YOUR FORM TO THE ABOVE ADDRESS.**

<b>1. REPORT DATE (DD-MM-YYYY)</b> xx-xx-2008		<b>2. REPORT TYPE</b> Technical Report		<b>3. DATES COVERED (From - To)</b> 1/1/2006-4/30/2008	
<b>4. TITLE AND SUBTITLE</b> Optically-gated Non-latched High Gain Power Device				<b>5a. CONTRACT NUMBER</b> N00014-06-1-0227	
				<b>5b. GRANT NUMBER</b>	
				<b>5c. PROGRAM ELEMENT NUMBER</b>	
<b>6. AUTHOR(S)</b> Sudip K Mazumder				<b>5d. PROJECT NUMBER</b>	
				<b>5e. TASK NUMBER</b>	
				<b>5f. WORK UNIT NUMBER</b>	
<b>7. PERFORMING ORGANIZATION NAME(S) AND ADDRESS(ES)</b> University of Illinois at Chicago				<b>8. PERFORMING ORGANIZATION REPORT NUMBER</b> E6542	
<b>9. SPONSORING/MONITORING AGENCY NAME(S) AND ADDRESS(ES)</b> Office of Naval Research 875 N Randolph St Arlington, VA 22203-1995				<b>10. SPONSOR/MONITOR'S ACRONYM(S)</b>	
				<b>11. SPONSORING/MONITORING AGENCY REPORT NUMBER</b>	
<b>12. DISTRIBUTION AVAILABILITY STATEMENT</b>					
<b>13. SUPPLEMENTARY NOTES</b>					
<b>14. ABSTRACT</b> GaAs based optically-trigegred power transistor (OTPT) has been developed for fast, repetitive, non-latched switching and control of power semiconductor device (PSD) for power electronics applications. OTPT has been coupled to different PSDs and overall switching dynamics is shown to be controlled by optical intensity modulation. Scalability of this concept over a wide range of PSDs has been demosntrated. Power electronics system level parameters such as power conversion efficiency, dv/dt and di/dt stress on PSD and electromagnetic noise emission spectrum, which depend directly on the switching dynamics of PSD, are also shown to be optically modulated. Experimental validations are presented along with theoretical anlyses for each major milestone.					
<b>15. SUBJECT TERMS</b> Optically-trigegred, GaAs, SiC, optical modulation, power semiconductor device, electromagnetic noise					
<b>16. SECURITY CLASSIFICATION OF:</b>			<b>17. LIMITATION OF ABSTRACT</b> UU	<b>18. NUMBER OF PAGES</b> 62	<b>19a. NAME OF RESPONSIBLE PERSON</b>
<b>a. REPORT</b> C	<b>b. ABSTRACT</b> U	<b>c. THIS PAGE</b> U			<b>19b. TELEPONE NUMBER (include area code)</b>

**20090109117**

# **Optically-gated Non-latched High Gain Power Device**

## **Final Report**

Award No: N00014-06-1-0227

November 21<sup>st</sup>, 2008

**Sudip K. Mazumder, Ph.D.**

Director, Laboratory for Energy and Switching-Electronics System  
Associate Professor, Department of Electrical and Computer Engineering  
University of Illinois at Chicago  
851 South Morgan Street  
Science and Engineering Office, Room No. 1020  
Mail Code 154, Chicago, IL: 60607-7053  
E-mail: [mazumder@ece.uic.edu](mailto:mazumder@ece.uic.edu)  
Phone: 312-355-1315  
Fax: 312-996-6465



## TABLE OF CONTENTS

<b>1. INTRODUCTION.....</b>	<b>4</b>
1.1 Project goal .....	4
1.2 Optical triggering – electromagnetic interference immunity and optical modulation of system performance .....	4
1.3 Summary of work up to the first annual report (July 2006) .....	7
1.4 Summary of research issues and tasks covered during August 2006-August 2007 .....	7
1.5 Summary of research issues and tasks covered during August 2007-April 2008.....	7
<b>2. INVESTIGATION OF THE EFFECT OF OPTICAL INTENSITY MODULATION.....</b>	<b>8</b>
2.1. Optically-triggered power transistor structure .....	9
2.2 On-state resistance ( $R_{on}$ ) of OTPT modulated by optical power density.....	10
2.3 Switching times modulated by optical power density .....	13
<b>3. HIGH GAIN EPITAXIAL GROWTH-BASED STRUCTURE, PHYSICS-BASED SIMULATION, AND FABRICATION PROCESS-FLOW DESIGN.....</b>	<b>16</b>
3.1. Epitaxial growth-based structure and operation .....	16
3.2. Numerical simulation framework and optical intensity modulation.....	19
3.3. Key design considerations .....	21
3.3. Photomasks for the fabrication of 2nd generation prototype.....	23
3.4. Low-doped epi growth for high voltage blocking .....	26
3.5. Process-flow for the fabrication of 2 <sup>nd</sup> generation prototype.....	27
3.6 Packaging details for the prototype.....	32
<b>4. EXPERIMENTAL STUDIES ON OTPT AND OPTICAL INTENSITY MODULATION OF OTPT PARAMETERS .....</b>	<b>33</b>
4.1 Optical source, driver, and fiber details .....	33
4.2. Switching experimental setup .....	33
4.3. Dark resistivity of OTPT .....	34
4.4. Nominal switching and pulse-following characterizations.....	34
4.5. Turn-on and turn-off dynamics characterizations.....	36
4.5. Optical intensity modulation of OTPT parameters.....	37
<b>5. EXPERIMENTAL STUDIES ON HYBRID OTPT-PSD AND OPTICAL INTENSITY MODULATION OF PSD SWITCHING DYNAMICS.....</b>	<b>39</b>
5.1. Optically-modulated Active Gate Control (OMAG) architecture for full controllability of turn-on and turn-off dynamics of PSD.....	39
5.3. Relationship between PSD switching parameters and optical intensity .....	41
5.4. Experimental characterization of optical intensity modulation of switching dynamics ....	42
5.5. Scalability of optical control with respect to PSD .....	45
5.6. Integrated packaging of GaAs OTPT with different types of PSDs.....	49
<b>6. OPTICAL INTENSITY MODULATED SYSTEM PERFORMANCE PARAMETERS.....</b>	<b>50</b>
6.1. Optical intensity modulation of power conversion efficiency .....	51



6.2. Optical intensity modulation of $dv/dt$ and $di/dt$ stress .....	53
6.3. Optical intensity modulation of electromagnetic noise .....	55
<b>7. SUMMARY OF THE PROJECT TASKS AND RESEARCH FINDINGS.....</b>	<b>58</b>
7.1. Summary of the work.....	58
7.2. Key research findings .....	58

# 1. INTRODUCTION<sup>1</sup>

## 1.1 Project goal

To design, fabricate and characterize a non-latched, high-gain optically-triggered power transistor for fast repetitive switching for power electronics applications.

## 1.2 Optical triggering – electromagnetic interference immunity and optical modulation of system performance

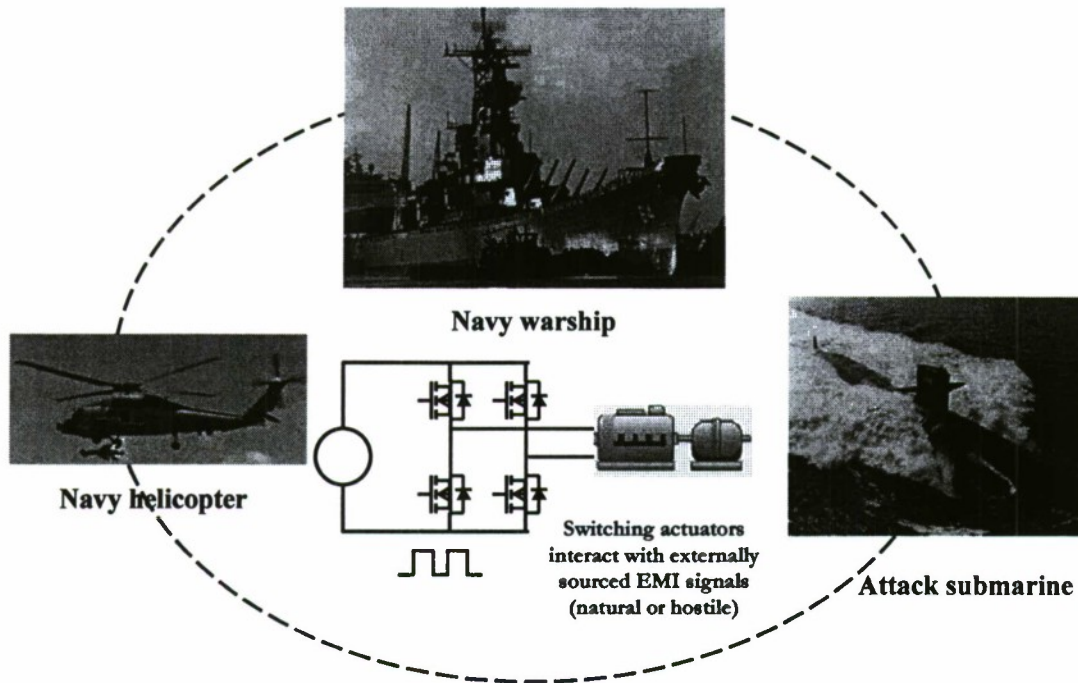
Electric actuation is one of the major enabling technologies for achieving the all-electric warships and naval warfare systems [1]. In an environment where external radio-frequency (RF) signals can interact with power electronics (shown in Fig. 1), for example *fly-by-light* (FBL) architecture for next- generation avionics, electromagnetic interference (EMI) is a critical issue [2, 3]. EMI immunity of these actuators from external jamming signals (often in the form of radio-frequency (RF) wave) could be a critical countermeasure for US naval force. EMI-immune countermeasure technology can be used in EMI-resistant naval ship-, submarine, on-board flight-control systems, and naval planes and helicopters. For example, optical control, actuation and sensing are promising methods for enhancing EMI-immunity. Sail-by-light (SBL) and fly-by-light (FBL) ship- and flight-control technologies not only improve the EMI tolerance of ship, submarine, and aircraft electronics, they also reduce system weight, volume, and cost, largely due to the reduced shielding requirements of distributed control and communication bus of copper wiring, which is replaced by lightweight optical fiber. For instance, published reports [3] assert that FBL technology (and on a similar note SBL technology) can cut flight control system weight by approximately 25%, volume by about 30%, cooling by nearly 40%, and cost by about 25%. In this respect, next-generation photonic power-electronic systems, based on optically-triggered devices (OTDs) [4-8] provide key advantages over conventional electrically-triggered device (ETD) based switching power electronics.

The prospective applications for such an EMI-immune power device include power management systems in military and commercial aircrafts, spacecrafts, electric warships, naval planes and helicopters, battle tanks, armored cars, field artillery vehicles. In short, any military or commercial automotive electric power management system, which may be affected by intentional or unintentional RF/EMI signal, may have the need of such device. The advantage of complete electrical isolation between driver and power stage also extends the possible applications areas of device into i) flexible AC transmission systems, ii) active power filters, iii) motor drives, iv) telecommunication, v) distributed generation.

During the course of the execution of this project, another critically important application of optical control of power device was realized. That is the optical intensity modulation of power semiconductor device switching dynamics and resulting modulation of system level performance parameters.

---

<sup>1</sup> The contents of this report are protected by the following University of Illinois, Chicago Intellectual Property: 1) S.K. Mazumder and T. Sarkar, "Optically-triggered power system and devices", U.S. Patent Application Number 11/922,185, filed on December 12, 2007. Original provisional patent application filed CY083 filed in September 2005. 2) S.K. Mazumder and T. Sarkar, "Optically-triggered multi-stage power system and devices", filed on June 11, 2008. Addendum patent application with regard to patent application cited in "1".



**Fig. 1: Switching power converter in navy combat vehicles and interaction with EMI.**

A power-electronic system is essentially a power-processor which takes electrical power input in a certain form and delivers electrical power output in a different form. These forms could indicate the attributes of the electrical quantities such as voltage and current magnitude or their time-dependent functional structure. A modern power-electronic system typically comprises of semiconductor switches, passive magnetic and electrostatic energy storage components (inductor, transformer, and capacitor for example), control logic electronics, etc. It has been noted that converter technology has been advanced largely by improvement in power semiconductor device (PSD) technology. The primary function of a PSD is to switch power from the input source to the output load in a controlled fashion.

There can be various measures of performance for a power-electronic systems, one of the most important being power conversion efficiency, which indicates the degree to which the system is transferring the input energy (or power) to the output in a processed form without losing a significant fraction of the energy in this transformation process. Furthermore, reliability of a power-electronic system is also of paramount importance and the electrical stress levels on the PSD and other components are among the primary determinants of that reliability. Fast time-dependent changes in voltage and current levels at different nodes of the electrical circuit, coupled with magnetic and electrostatic elements (either discrete components or distributed in the circuit layout) often give rise to such stresses.

Switching dynamics of PSD can be linked to power conversion efficiency (governing factor being the switching loss) and transient-induced voltage and current stress (governing factor being rate of change of voltage and current). Therefore, it follows logically that by controlling the switching dynamics at the device level, some performance parameters and reliability aspects of a power-electronic system can be controlled (as illustrated in Fig. 2). Those parameters could be,



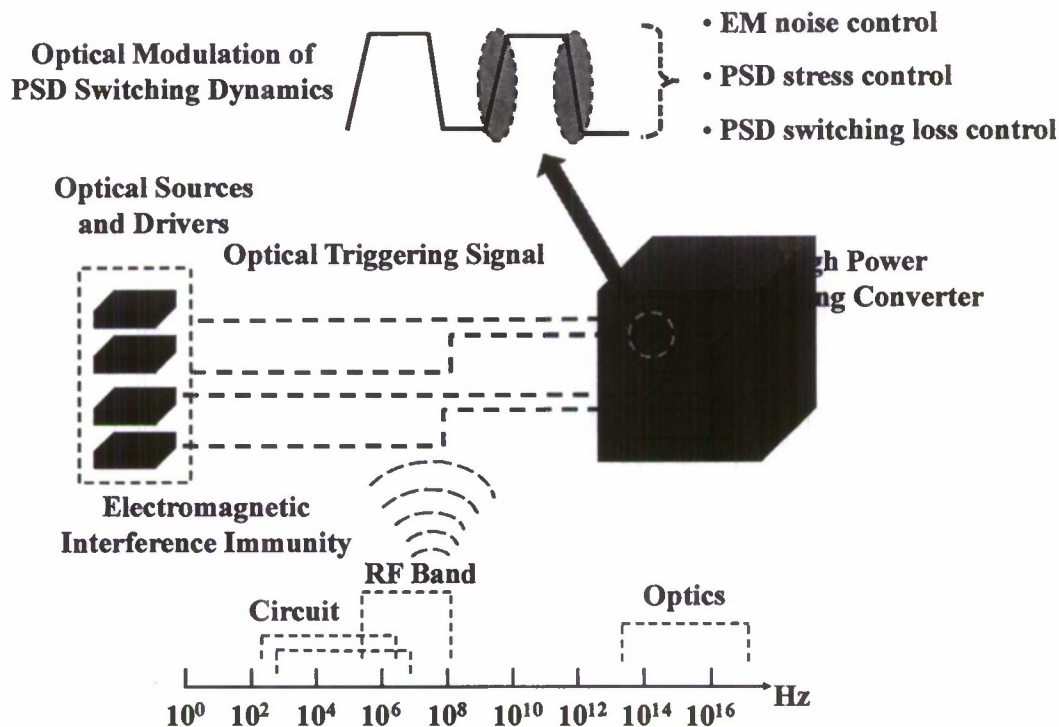


Fig. 2: Optically-triggered device based power electronics system with reduced susceptibility to external EMI signals as well as having the feature of optical modulation of system performance.

- Power conversion efficiency
- Device stress by fast rate of change of voltage and current
- Electromagnetic noise generated by fast switching phenomena in the power converter

Active gate control (AGC) of PSDs is a technique in power electronics which is typically achieved by modulating the switching dynamics of PSDs to control aforementioned system-level performance parameters. Aim of the current research is to achieve AGC with optical modulation. Functionally, optical control of the PSD exists in current power electronics technology in the form of optical isolation techniques for gate driver signals. Electrical gate control signals are converted into optical signals and are transmitted over fiber. At the receiving end they are converted back to electrical logic signals which activate gate driver which eventually drives the PSD. This optical control, therefore, enhances immunity to external electromagnetic noise and provides galvanic isolation between power stage and control electronics. Optical intensity modulated gate control therefore achieves optical isolation and dynamic control of above-mentioned system-performance parameters through a unified scheme (Fig. 2). *The outcome of the optical modulation is the integration of the pulse-width-modulation (PWM) information, which is typically required for control regulation of power converters, with the optical amplitude modulation that affects the switching dynamics of a PSD.*

### ***1.3 Summary of work up to the first annual report (July 2006)***

- Initial device design and optimization was completed including epitaxial charge-balance mechanisms and robustness studies. Effect on device performance parameters due to variation in processing was also investigated in detail.
- Fabrication of the 1<sup>st</sup> generation prototype device was completed based on the design insights obtained from the optimization study.
- Wafer level testing was done on the prototype device for steady-state characterizations.
- Test-bed design for switching characterizations was started. The aim was to demonstrate non-latched, fast repetitive switching using 800 nm wavelength laser source.

### ***1.4 Summary of research issues and tasks covered during August 2006-August 2007***

- Detailed investigation of the effect of dynamic variation of power density, wavelength, and switching time on the properties of optically-triggered power transistor was required. This was carried out by analytical modeling and two-dimensional physics based numerical simulation.
- Fabrication and characterization of 1<sup>st</sup> generation optically-triggered power transistor prototype was critical for experimentally demonstrating the non-latched, fast repetitive switching action of the device. For the device testing, a comprehensive laser test-bed was designed that can produce optical triggering signal of varying intensity, frequency, duty-cycle with spherically uniform output wavefront. Laser source, corresponding driver, and calibrating photodetector were procured and set up.
- The prototype device was packaged along with fiber-coupling feature. This included wafer cleaning, die separation, die attachment, wire-bonding, hermetic sealing, and optical fiber interfacing.
- Optical activation was tested experimentally. Non-latched fast repetitive switching behavior was experimentally demonstrated for various frequencies and over a wide range of duty-cycle. Effect of variation of optical triggering power on the device switching properties (rise and fall time, turn-on and turn-off delay, and on-state drop) were characterized experimentally and results were found to be matching with earlier theoretical predictions.
- For the fabrication of 2<sup>nd</sup> generation prototype, based on the initial characterization of double-implanted GaAs test samples, it was concluded that degree of activation for simultaneous implanted GaAs is a potential issue. To solve this problem, a revised structure was designed replacing double-implanted regions by epitaxially grown and suitably patterned layers.
- For the fabrication of 2<sup>nd</sup> generation device, CAD drawings of the photomasks have been finalized and reticules have been fabricated. Process-flow designs have been completed. Growth of the revised epitaxial structure has been completed. Processing has been started. Packaging details are being finalized following the procedure of packaging of 1<sup>st</sup> generation device.

### ***1.5 Summary of research issues and tasks covered during August 2007-April 2008***

- Fabrication processing of the 2<sup>nd</sup> generation optical-triggered power transistor (OTPT) has been completed.



- Packaging (with optical interfacing) of the 2nd generation OTPT has been completed.
- Detailed experimental characterizations of the OTPT have been performed with regard to pulse-following capability and modulation of switching times with optical power.
- OTPT has been integrated with different power semiconductor devices (PSD) and detailed switching characterizations have been carried out to investigate the effect of optical intensity modulation on switching dynamics of the PSD.
- Prototype power converter has been fabricated into which the optically-controlled PSD is integrated to investigate the effect of optical intensity modulation on the system level performance parameters. It is shown that critical system parameters such as power conversion efficiency, electromagnetic (EM) noise, and transient stress (dv/dt and di/dt related) on the PSD can be modulated by optical intensity variation.
- An optimization problem has been identified with regard to system parameter modulation and corresponding future research directions have been critically discussed.

## 2. INVESTIGATION OF THE EFFECT OF OPTICAL INTENSITY MODULATION

Optical modulation by varying the intensity, wavelength, or switching time can dynamically alter the performance parameters of direct optically-controlled power semiconductor device. Understanding the effect of optical parameters on these parameters from a first principle approach is necessary for making optimal design choices and gaining design insights. We focus on performance parameters whose variations with direct optical modulation have not been reported previously for a power semiconductor such as switching times and on-state resistance.

Use of optical modulation techniques for power semiconductors have primarily been applied for measurement, reliability analysis, and characterization techniques [9, 10] but not as means of dynamically altering device performance parameters. On the other hand, research on optical modulation and control of other conventional electrical devices like MOSFET [11, 12], MESFET [13-15], or HEMT [16] have primarily concentrated on microwave systems, low-power signal detection, and optical communication applications which have different requirements from power semiconductor devices and associated power electronics applications. The common feature of these works is that optical signal was applied to modulate steady-state properties such as I-V characteristic [11, 12, 14], RC time constant [15], RF s-parameters [13], or pinch-off voltage [16] which are very important from the corresponding application area point of view but do not cover the direct modulation aspects of switching properties like rise and fall time, which are important in power electronics applications. Moreover, modulations are reported mainly with respect to the power of the optical signal and not on optical wavelength. For fast switching direct optically-controlled power semiconductors, nonlinear variation of reflectivity and optical absorption coefficient with wavelength demands an optimum operating wavelength to be investigated. Wavelength dependent photogenerated current density and optical power dependent drain-source current for optically-controlled bipolar mode field-effect transistor (BMFET) were reported in [17, 18] but an explicit description of the variation of on-state resistance and switching time with varying wavelength or optical power was not given. Also, no study was reported describing how the switching characteristic of BMFET will depend on the switching times of the optical signal. The rise and fall time for a direct optically-controlled power device depends on the switching times of corresponding optical triggering signal and a study is required



to estimate how the variation in rise time of the triggering optical signal may affect that of the main power device.

Another category of research studies in this particular area deals with electrically-gated main power device being indirectly controlled by optical signals. Amplitude, wavelength, and pulse-width modulation strategies for optically triggered power DMOSFET (OT-MOS) were reported in [19] with Si power MOSFET and GaAs photodiode and photoconductive triggering structures. However, the power MOSFET being an electrically-gated device, the switching properties of OT-MOS are largely limited by junction and oxide capacitance of the MOSFET and exhibit less dependence on optical parameters than a direct optically-controlled device. Similar studies related to the switching times of an optically-controlled power bipolar junction transistor (BJT) is reported in [20] using light-emitting diode (LED)-phototransistor pair as the driving circuit. Si phototransistor controlled SiC Darlington BJT has been proposed [21] for FBL applications but not much details on the optical modulation is provided.

### 2.1. Optically-triggered power transistor structure

We show in Fig. 3, the structural schematic of the OTPT. It has a lateral structure with two electrodes - source and drain. The optical window is defined by the anti-reflecting layer between the electrodes. The bottom  $P$ -type GaAs layer acts as the charge-compensating layer and the doping and thickness values of the epitaxial layers, that is  $d_1$ ,  $d_2$ ,  $N_{\text{drift}}$ ,  $N_2$ , have been designed such as to realize the superjunction charge-balance [5], i.e., the total positive charge contributed by  $P$ -GaAs layer nullifies the total negative charge contributed by the top  $N$ -type layers. The OTPT structure features a deep-implanted  $P$ -body which may extend all the way up to the  $P$ -GaAs layer. The junction between the  $P$ -body and the  $N$ -drift region results in almost ideal parallel-plate like electric field distribution during blocking state.

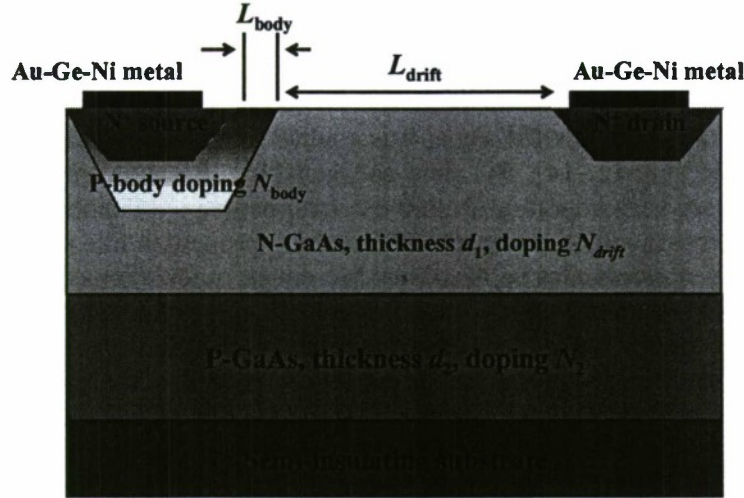


Fig. 3: Structural schematic of the OTPT.

In the blocking or open state, the applied voltage is supported by the reverse biased  $P$ - $N$  junction between the  $P$ -body and  $N$ -drift regions. When triggering light beam falls on the device, in the optical window region it is absorbed and it generates electron-hole plasma by

photogeneration. They are mobilized by the local electric field and are attracted by the drain and source electrodes and constitute electron and hole currents thereby closing the switch. If the light beam is sustained the conductivity is sustained too and the switch remains closed. When the light shuts off, the carriers are recombined among themselves and the switch goes back to its high-resistivity blocking state.

## 2.2 On-state resistance ( $R_{on}$ ) of OTPT modulated by optical power density

For estimation of  $R_{on}$  we need to obtain steady-state carrier concentration by solving continuity equation. Fig. 4 demonstrates that current densities in  $x$ -direction are much higher compared to that in  $y$ -direction and therefore we focus on one-dimensional continuity equation whose general form for electron and hole are as follows,

$$\frac{\partial n}{\partial t} = D_n \frac{\partial^2 n}{\partial x^2} + \mu_n E \frac{\partial n}{\partial x} + G - R; \quad \frac{\partial p}{\partial t} = D_p \frac{\partial^2 p}{\partial x^2} + \mu_p E \frac{\partial p}{\partial x} + G - R \quad (1)$$

where  $E$  denotes electric field,  $n, p$  are electron and hole densities,  $D_n, D_p$  are electron and hole diffusion coefficients,  $\mu_n, \mu_p$  are electron and hole mobilities,  $G$  is the generation rate and  $R$  is the total recombination rate. We assume that both Shockley-Read-Hall (SRH) and radiative band-to-band direct recombination occurs in OTPT because of the direct bandgap nature of GaAs. SRH recombination rate is given by [22],

$$R_{n,SRH} = v_{th} \sigma_o N_t \frac{pn - n_i^2}{p + n + 2n_i \cosh\left(\frac{E_t - E_i}{kT}\right)} = R_{p,SRH} \quad (2)$$

where  $R_{n,SRH}$  and  $R_{p,SRH}$  are electron and hole SRH recombination rates,  $v_{th}$  is thermal velocity,  $\sigma_o$  is common capture cross-section,  $N_t$  is the trap centre density,  $E_t$  is the trap energy level,  $E_i$  is the equilibrium energy level,  $n_i$  is the intrinsic carrier density,  $k$  is the Boltzmann constant and  $T$  is the absolute temperature.

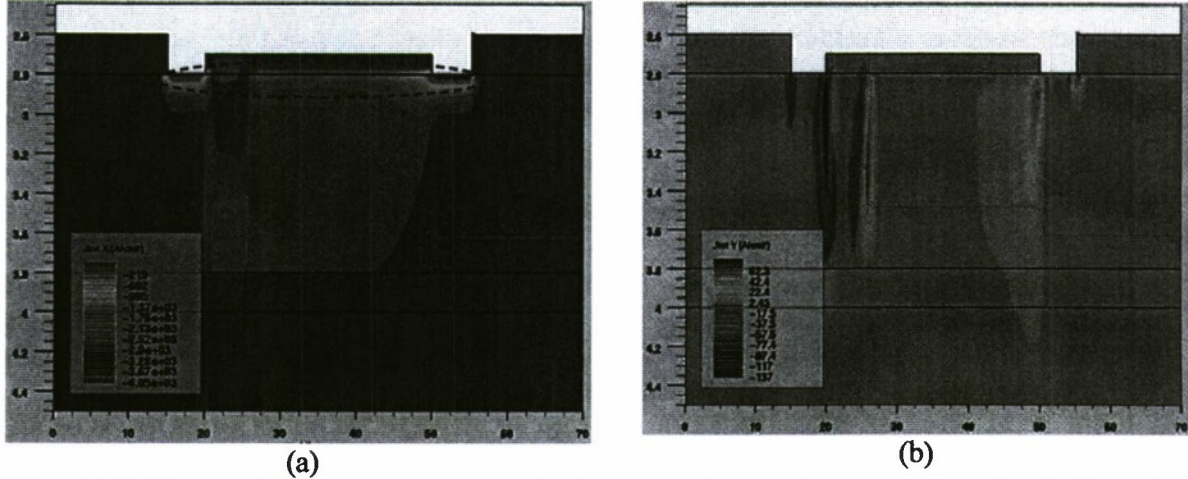
For OTPT, typical doping density in the P-body region is  $\sim 10^{17} \text{ cm}^{-3}$  and in the N-drift region is  $\sim 10^{14} \text{ cm}^{-3}$  whereas the GaAs intrinsic carrier density is  $2.1 \times 10^6 \text{ cm}^{-3}$ . Clearly, the product  $pn \gg n_i^2$  for any region of the device and we can neglect the contribution from the  $n_i$  related terms. Therefore, SRH recombination rate can be re-written as,

$$R_{n,SRH} = \frac{pn}{p + n} \left( \frac{1}{1/v_{th} \sigma_o N_t} \right) = \frac{pn}{(p + n) \tau_{nH}} \quad (3)$$

where  $\tau_{nH} = 1/v_{th} \sigma_o N_t$  is the high-level injection lifetime for electron. There can be two levels of injection (external carrier entering into the device active regions). They are as follows,

1. **High-level injection:** where the injected carrier density is comparable to the already existing doping density of that region;
2. **Low-level injection:** where the injected carrier density is negligible compared to the already existing doping density of that region.





**Fig. 4:** Total current density (negative value because of majority electron conduction) in the OTPT during conduction state in (a)  $x$ -direction and (b)  $y$ -direction. The photogenerated channel is indicated by the high current density (dotted ellipse) near the surface in (a).

High-level injection assumption transforms (1) into a nonlinear second-order differential equation whose closed-form analytical solution cannot be obtained. But we can transform the mobility and diffusion coefficient values to take into account simultaneous presence of both electron and holes in high degree. We use ambipolar mobility ( $\mu_a$ ) and diffusion coefficients ( $D_a$ ) instead of separate electron and hole mobility and diffusion coefficients. They are defined as follows,

$$\mu_a = \frac{\mu_n \mu_p}{\mu_n + \mu_p}; D_a = \frac{\mu_p D_n + \mu_n D_p}{\mu_n + \mu_p} \quad (4)$$

Therefore we can make the low-level injection assumption i.e. the photogenerated carrier density is considerably less than the doping density in the P-type region. In that case, we can rewrite (2) as,

$$R_{n,SRH} = \frac{pn}{p+n} \left( \frac{1}{1/v_{th} \sigma_o N_t} \right) = \frac{n}{\left( \frac{p+n}{p} \right) \tau_{nH}} \approx \frac{n}{\tau_{nL}} \quad (5)$$

Similarly, we obtain  $R_{p,SRH} \approx \frac{p}{\tau_{pL}}$ . Here,  $\tau_{nL}$  and  $\tau_{pL}$  are low-level lifetimes for electrons and holes.

The radiative recombination rate  $R_{rad}$  is same for electrons and holes and is given by [22],

$$R_{rad} = C_d (pn - n_i^2) \quad (6)$$

where  $C_d$  is the radiative recombination coefficient. The photogeneration rate is same for electrons and holes and is given by [22],

$$G_n(y) = G_p(y) = \eta(1-R) \frac{P\lambda}{hc} \alpha e^{-\alpha y} = G(y) \quad (7)$$

where,  $\eta$  is the quantum efficiency,  $R$  is the surface reflectivity of the semiconductor,  $P$  is the optical power density i.e. power incident on unit area,  $\lambda$  is the wavelength of the optical beam,  $\alpha$  is the optical absorption coefficient,  $h$  and  $c$  denote Planck's constant and velocity of electromagnetic wave respectively.

For steady-state analysis the time-dependent left-hand term in (1) is zero. Therefore, (1) transforms into a linear ordinary differential equation,



$$0 = D_a \frac{d^2 n}{dx^2} + \mu_a E \frac{dn}{dx} + G(y) - (R_{n,SRH} + R_{rad}) \quad (8)$$

Similar equation can be written for holes. Using (5), (6), and (7) in (8), we obtain the second order ordinary differential equations governing the minority carrier densities i.e. electron and hole concentrations in P-body and N-drift regions as,

$$D_a \frac{d^2 n}{dx^2} + \mu_a E \frac{dn}{dx} - \left( \frac{1}{\tau_{nL}} + C_d N_{body} \right) n = -[G(y) + C_d n_i^2] \quad (9-a)$$

$$D_a \frac{d^2 p}{dx^2} + \mu_a E \frac{dp}{dx} - \left( \frac{1}{\tau_{pL}} + C_d N_{drift} \right) p = -[G(y) + C_d n_i^2] \quad (9-b)$$

where  $N_{body}$  and  $N_{drift}$  are majority carrier densities in P-body and N-drift regions respectively. The solutions of (11) can be given as,

$$n(x) = K_1 e^{m_1 x} + K_2 e^{m_2 x} + \frac{G(y) + C_d n_i^2}{\left( \frac{1}{\tau_{nL}} + C_d N_{body} \right)}; p(x) = K_3 e^{m_3 x} + K_4 e^{m_4 x} + \frac{G(y) + C_d n_i^2}{\left( \frac{1}{\tau_{pL}} + C_d N_{drift} \right)} \quad (10)$$

In (10),  $K_1$ - $K_4$  are the constants to be determined from boundary conditions and so are dependent on specific geometry and doping definition of the device. The other constants are defined as following:

$$m_1, m_2 = \frac{(-\mu_a E) \pm \sqrt{(\mu_a E)^2 + 4D_a \left( \frac{1}{\tau_{nL}} + C_d N_{body} \right)}}{2D_a}; m_3, m_4 = \frac{(-\mu_a E) \pm \sqrt{(\mu_a E)^2 + 4D_a \left( \frac{1}{\tau_{pL}} + C_d N_{drift} \right)}}{2D_a} \quad (11)$$

For P-body and drift region, we calculate the averaged minority carrier densities as follows,

$$n_{body} = \frac{\int_0^{L_{body}} n(x) dx}{L_{body}} = \frac{m_1 K_1 e^{m_1 L_{body}} + m_2 K_2 e^{m_2 L_{body}} - (K_1 m_1 + K_2 m_2)}{L_{body}} + \frac{G(y) + C_d n_i^2}{\left( \frac{1}{\tau_{nL}} + C_d N_{body} \right)} \quad (12-a)$$

$$p_{drift} = \frac{\int_0^{L_{drift}} p(x) dx}{L_{drift}} = \frac{m_3 K_3 e^{m_3 L_{drift}} + m_4 K_4 e^{m_4 L_{drift}} - (K_3 m_3 + K_4 m_4)}{L_{drift}} + \frac{G(y) + C_d n_i^2}{\left( \frac{1}{\tau_{pL}} + C_d N_{drift} \right)} \quad (12-b)$$

where  $L_{body}$  and  $L_{drift}$  denote the length of P-body and N-drift regions respectively. Two main components of the overall  $R_{on}$  are the P-body resistance ( $R_{body}$ ) and N-drift resistance ( $R_{drift}$ ) resulting in

$$R_{on} = R_{body} + R_{drift} = \frac{L_{body}}{q \int_0^{d_1} n_{body} \mu_a Z dy} + \frac{L_{drift}}{q \int_0^{d_1} p_{drift}(x) \mu_a Z dy} \quad (13)$$

where  $q$  is the electronic charge,  $Z$  is the width of the device in Z-direction (perpendicular to the plane of the paper). Using the photogeneration function from (7), doing the integration, and substituting (12-a) and (12-b) in (13) we can write  $R_{on}$  in a compact form,

$$R_{on} = \frac{C_1 L_{body}}{C_1 + C_1^* P} + \frac{C_2 L_{drift}}{C_2 + C_2^* P} \quad (14)$$

where,

$$C_1 = \frac{1}{qZ\mu_a} = C_2 \quad (15-a)$$

$$C_1' = \left[ \frac{m_1 K_1 e^{m_1 L_{body}} + m_2 K_2 e^{m_2 L_{body}} - (K_1 m_1 + K_2 m_2)}{L_{body}} + \frac{C_d n_i^2}{\left( \frac{1}{\tau_{nL}} + C_d N_{body} \right)} \right] d_1 \quad (15-b)$$

$$C_2' = \left[ \frac{m_3 K_3 e^{m_3 L_{drift}} + m_4 K_4 e^{m_4 L_{drift}} - (K_3 m_3 + K_4 m_4)}{L_{drift}} + \frac{C_d n_i^2}{\left( \frac{1}{\tau_{pL}} + C_d N_{drift} \right)} \right] d_1 \quad (15-c)$$

$$C_1^* = \frac{\eta(1-R)\lambda(1-e^{-\alpha d_1})}{hc \left( \frac{1}{\tau_{nL}} + C_d N_{body} \right)}; C_2^* = \frac{\eta(1-R)\lambda(1-e^{-\alpha d_1})}{hc \left( \frac{1}{\tau_{pL}} + C_d N_{drift} \right)} \quad (15-d)$$

### 2.3 Switching times modulated by optical power density

Transient modeling of the OTPT dynamics requires time-dependent carrier density calculation as a function of optical power density. The P-body region is critical in determining the transient dynamics because it strongly influences the recombination rate. At first, we consider high-level injection case. The diffusion terms involving  $\partial n / \partial x$  and its derivative in (1) can be considered negligible (because of uniform carrier density in the P-body region) and we can write the time-varying equation in the P-body region as,

$$\frac{dn}{dt} = G_{opt} - \frac{N_{body} n}{(N_{body} + n)\tau_{nH}} - C_d (N_{body} n - n_i^2) \quad (16)$$

Ion implantation was done to realize the P-body region in the fabricated prototype and in that case the average acceptor density can be given as,

$$N_{body} = \frac{\int_0^{R_{body}} \frac{Q_{body}}{\Delta R_{body} \sqrt{2\pi}} \exp \left[ -\frac{(y - R_{body})^2}{2\Delta R_{body}^2} \right] dy}{R_{body}} \quad (17)$$

where,  $Q_{body}$  is implantation dose for P-body,  $R_{body}$  is implant range for P-body (for a particular species of ion), and  $\Delta R_{body}$  is lateral struggle for P-body implantation. The spatially averaged photogeneration rate  $G_{opt}$  can be given as,

$$G_{opt} = \frac{\int_0^{d_1} G(y) dy}{\int_0^{d_1} dy} = \eta(1-R) \frac{P\lambda}{hc} \left( \frac{1-e^{-\alpha d_1}}{d_1} \right) \quad (18)$$

where photogeneration rate (which varies with the depth) is averaged over the thickness ( $d_1$ ) of the optical absorption layer i.e. N-GaAs layer. Separating the variables in (16), we obtain,

$$\int \frac{\tau_{nH} (N_{body} + n) dn}{-C_d \tau_n N_{body} n^2 + (G_{opt} \tau_{nH} - N_{body} - C_d N_{body}^2 \tau_{nH}) n + G_{opt} N_{body} \tau_{nH}} = \int dt \quad (19)$$

$$\begin{aligned} & \frac{1}{2C_d \tau_{nH} N_{body}} \ln \left[ -C_d \tau_{nH} N_{body} n^2 + (G_{opt} \tau_{nH} - N_{body} - C_d N_{body}^2 \tau_{nH}) n + G_{opt} N_{body} \tau_{nH} \right] + \\ & \left( N_{body} + \frac{G_{opt} \tau_{nH} - N_{body} - C_d \tau_{nH} N_{body}^2}{2C_d \tau_{nH} N_{body}} \right) \left[ \frac{\ln \left( \frac{2C_d \tau_{nH} N_{body} n + G_{opt} \tau_{nH} - N_{body} - C_d \tau_{nH} N_{body}^2 - \sqrt{(G_{opt} \tau_{nH} - N_{body} - C_d \tau_{nH} N_{body}^2)^2 + 4G_{opt} C_d \tau_{nH}^2 N_{body}^2}}{2C_d \tau_{nH} N_{body} n + G_{opt} \tau_{nH} - N_{body} - C_d \tau_{nH} N_{body}^2 + \sqrt{(G_{opt} \tau_{nH} - N_{body} - C_d \tau_{nH} N_{body}^2)^2 + 4G_{opt} C_d \tau_{nH}^2 N_{body}^2}} \right)}{\sqrt{(G_{opt} \tau_{nH} - N_{body} - C_d \tau_{nH} N_{body}^2)^2 + 4G_{opt} C_d \tau_{nH}^2 N_{body}^2}} \right] = \frac{t+k}{\tau_{nH}} \end{aligned} \quad (20)$$

We assume the initial condition  $n(t=0) = 0$  (because initially the electron concentration in the P-body region is negligibly small, e.g.  $n_i^2 / p \approx (2.1 \times 10^6)^2 / 10^{17} \approx 4.41 \times 10^{-5}$ ). The integration constant  $k$  is obtained as,

$$k = \tau_{nH} \left[ \frac{1}{2a} \ln(c) + \left( p - \frac{b}{2a} \right) \left( \frac{1}{\sqrt{b^2 - 4ac}} \right) \ln \left( \frac{b - \sqrt{b^2 - 4ac}}{b + \sqrt{b^2 - 4ac}} \right) \right] \quad (21)$$

where the constants  $a, b, c$  are given by,

$$\begin{aligned} a &= -C_d \tau_{nH} N_{body} \\ b &= G_{opt} \tau_{nH} - N_{body} - C_d \tau_{nH} N_{body}^2 \\ c &= G_{opt} N_{body} \tau_{nH} \end{aligned} \quad (22)$$

Therefore, using (21) in (20) and the definitions of (22), the final transcendental time-domain equation governing electron density can be written as,

$$\tau_{nH} \left[ \frac{1}{2a} \ln \left( \frac{an^2 + bn + c}{c} \right) + \left( p - \frac{b}{2a} \right) \left( \frac{1}{\sqrt{b^2 - 4ac}} \right) \ln \left( \frac{(2an + b - \sqrt{b^2 - 4ac})(b + \sqrt{b^2 - 4ac})}{(2an + b + \sqrt{b^2 - 4ac})(b - \sqrt{b^2 - 4ac})} \right) \right] = t \quad (23)$$

We calculate rise time from the switching simulations done using OTPT device model in a mixed circuit-device simulator. A resistive load circuit is used as shown in Fig. 5a. Rise time is defined as the time taken to reach the electron density from zero to 95% of its final value (as shown in Fig. 5b), which we denote as  $n_F$ . Final electron density value is determined by the circuit and we can approximately calculate that from the resistance of the OTPT. For example, we obtained  $0.2 \Omega$  resistance for a Z-direction length of  $5 \times 10^5 \mu m$ . The GaAs layer depth is  $1 \mu m$ . Thus, the cross-sectional area ( $A_c$ ) through which carriers are traveling is,  $(5 \times 10^5 \times 1) \mu m^2$  or equivalently  $(50 \times 10^{-4}) cm^2$ . The length of the P-body region is  $5 \mu m$ . The electron density can be calculated as,

$$n_F = \frac{L_{body}}{R_{on} A_c q \mu_a} = \frac{5 \times 10^{-4} cm}{0.2 \Omega \times (50 \times 10^{-4}) cm^2 \times 1.602 \times 10^{-19} C \times 2000 cm^2/V \cdot sec} = 1.56 \times 10^{15} cm^{-3}$$

The equation relating  $t_r$  and  $P$  can be given as



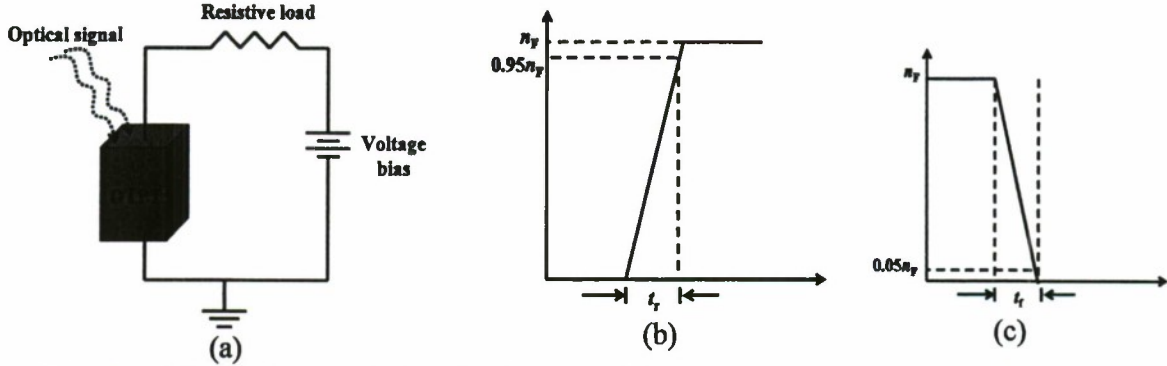


Fig. 5: (a) Switching simulation circuit and definitions of (b) rise time and (c) fall time.

$$t_r = \tau_{nH} \left[ \frac{1}{2a} \ln \left( \frac{a(0.95n_F)^2 + b(0.95n_F) + c}{c} \right) + \left( p - \frac{b}{2a} \right) \left( \frac{1}{\sqrt{b^2 - 4ac}} \right) \ln \left( \frac{(2a(0.95n_F) + b - \sqrt{b^2 - 4ac})(b + \sqrt{b^2 - 4ac})}{(2a(0.95n_F) + b + \sqrt{b^2 - 4ac})(b - \sqrt{b^2 - 4ac})} \right) \right] \quad (24)$$

$$t_r = \tau_{nH} \left[ \ln \left( \frac{M_1 P + M_2}{M_3 P} \right)^{M_4} + \frac{(M_5 P + M_6)}{\sqrt{M_7 P^2 + M_8}} \ln \left( \frac{M_9 P + M_{10} - \sqrt{M_7 P^2 + M_8}}{M_9 P + M_{10} + \sqrt{M_7 P^2 + M_8}} \right) \right] \quad (25)$$

where  $M_j$ ,  $j = 1, 2, \dots, 10$  are different constants that can be evaluated using (21), (22), and (24). We define fall-time as the time taken to reach the electron density to 5% of its final value (as shown in Fig. 5c) after the light is shut off. Therefore, for the OTPT turn-off, we can re-write (16) as,

$$\frac{dn}{dt} = -\frac{N_{body}n}{(N_{body} + n)\tau_{nH}} - C_d(N_{body}n - n_i^2) \quad (26)$$

Solving (26) in a similar manner and using the initial condition  $n(t=0) = n_F$ , we obtain the fall-time as,

$$t_f = \tau_{nH} \left[ S_1 + S_2 \ln \left( \frac{A n_F + B}{A(0.05n_F) + B} \right) \right] \quad (27)$$

where,  $A$ ,  $B$ ,  $S_1$  and  $S_2$  are constants and are given by,

$$A = C_d N_{body} \tau_{nH}; B = C_d N_{body}^2 \tau_{nH} + N_{body}; S_1 = \frac{N_{body} \ln(20)}{N_{body} + C_d N_{body}^2 \tau_{nH}}; S_2 = \frac{1}{C_d N_{body} \tau_{nH}} - \frac{N_{body}}{N_{body} + C_d N_{body}^2 \tau_{nH}} \quad (28)$$

Apparently  $P$  does not influence  $t_f$ , but because the final electron density in conduction state is influenced by the optical power density (as apparent from the  $R_{on}$  variation with  $P$  following the analysis in the previous sub-section), it does have an effect on the fall-time.

The closed-form solution of (16) can be considerably simplified in the low-level injection case where the equation changes to,

$$\frac{dn}{dt} = G_{opt} - \frac{n}{\tau_{nL}} - C_d(N_{body}n - n_i^2) \quad (29)$$

Neglecting  $n_i^2$  compared to  $pn$  (as done before) and taking the same initial condition we can write the general solution of (29) as,

$$n(t) = \frac{G_{opt}}{\left(\frac{1}{\tau_{nL}} + C_d N_{body}\right)} \left[ 1 - e^{-\left(\frac{1}{\tau_{nL}} + C_d N_{body}\right)t} \right] \quad (30)$$

Rise time can be calculated as,

$$t_r = \frac{\tau_{nL}}{1 + \tau_{nL} C_d N_{body}} \ln \left( \frac{G_{opt}}{G_{opt} - \left(\frac{1}{\tau_{nL}} + C_d N_{body}\right)(0.95 n_F)} \right). \quad (31)$$

We can write (31) in terms of  $P$  as,

$$t_r = F_1 \ln \left( \frac{F_2 P}{F_2 P - F_3} \right) \quad (32)$$

where  $F_1$ ,  $F_2$ , and  $F_3$  are constants and are given by,

$$F_1 = \frac{\tau_{nL}}{1 + \tau_{nL} C_d N_{body}}; F_2 = \eta(1-R) \frac{\lambda}{hc} \left( \frac{1 - e^{-\alpha d_1}}{d_1} \right); F_3 = \frac{(1 + \tau_{nL} C_d N_{body})(0.95 n_F)}{\tau_{nL}} \quad (33)$$

An interesting observation can be made from (25) and (32). The value of  $t_r$  in the limit of very large  $P$ , is zero as predicted by (32), because  $\lim_{P \rightarrow \infty} (t_r) = F_1 \ln \left( \frac{F_2 P}{F_2 P} \right) = 0$ . On the other hand, (25) predicts a small but finite value as,

$$\lim_{P \rightarrow \infty} (t_r) = \tau_{nH} \left[ \ln \left( \frac{M_1}{M_3} \right)^{M_4} + \left( \frac{M_5}{M_7} \right) \ln \left( \frac{M_9 - M_7}{M_9 + M_7} \right) \right] \quad (34)$$

This is more realistic because physically when the generation is very large, so is the recombination rate and there must be a finite time for the carrier density to reach the steady-state value.

### 3. HIGH GAIN EPITAXIAL GROWTH-BASED STRUCTURE, PHYSICS-BASED SIMULATION, AND FABRICATION PROCESS-FLOW DESIGN

#### 3.1. Epitaxial growth-based structure and operation

Some modifications were made in the 2<sup>nd</sup> generation device structure for achieving higher gain than the initially designed 1<sup>st</sup> generation prototype. The double implantation region (as shown in the Fig. 6a) is replaced by epitaxially grown layers of N<sup>+</sup> and P-GaAs (as shown in Fig. 6b). This was done due to the following reasons,

- The damage due to double implantation at the same region (P-type implant followed by N-type implant) could be high and the subsequent annealing might not be able to activate the implanted species as per the desired doping level.
- In the structure of Fig. 6b, the effective P-body length for the carriers traveling from the N<sup>+</sup> source to drain is dependent on the thickness of the P-GaAs layer, which can be controlled very precisely by epitaxial growth method. The doping density of this layer, which determines the effective lifetime of the photogenerated carriers (and thereby influences the

overall device gain), can also be more precisely controlled in the growth than that could be achieved using implant activation.

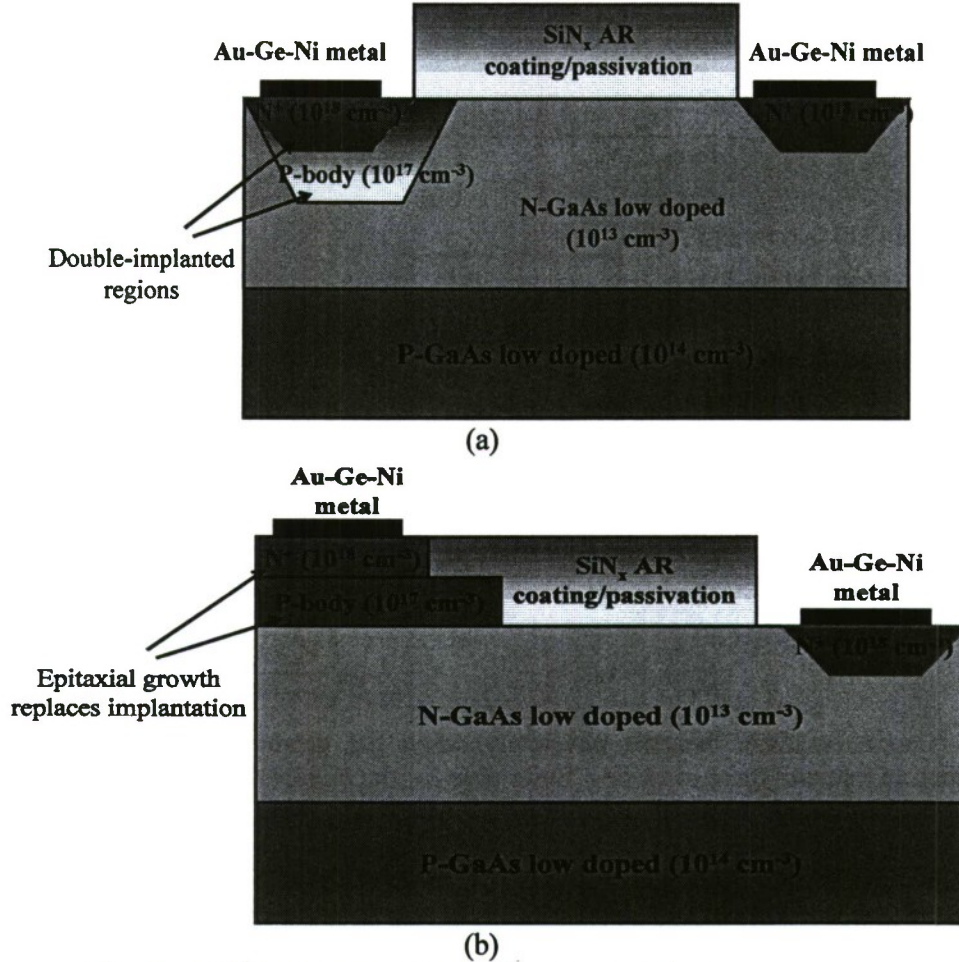


Fig. 6: (a) 1<sup>st</sup> generation and (b) 2<sup>nd</sup> generation device prototype.

In the blocking or open state, the applied voltage is supported by the reverse biased P-N junction between the P-base and N-drift regions. The electric field distribution at the instant of breakdown is shown in Fig. 7. When triggering light beam falls on the device, in the optical window region it is absorbed and electron-hole plasma is generated by photogeneration (as shown in Fig. 8). These electron-hole pairs are mobilized by the local electric field and are attracted by the drain and source electrodes and constitute electron and hole currents thereby closing the switch (as illustrated in Fig. 9). If the light beam is sustained, conductivity remains high and the switch remains closed. When the light shuts off, the carriers are recombined among themselves and the switch goes back to its high-resistivity blocking state. The device gain (defined as the ratio between the drain current and photogenerated current) and the switching speed of OTPT depends strongly on the minority carrier recombination lifetime in the P-base region. A shorter lifetime ensures faster turn-off due to rapid recombination when the light shuts off, but it also leads to low device gain because a larger fraction of the photogenerated carriers



gets recombined before reaching the drain or source terminals. A design trade-off may be necessary depending upon particular application.

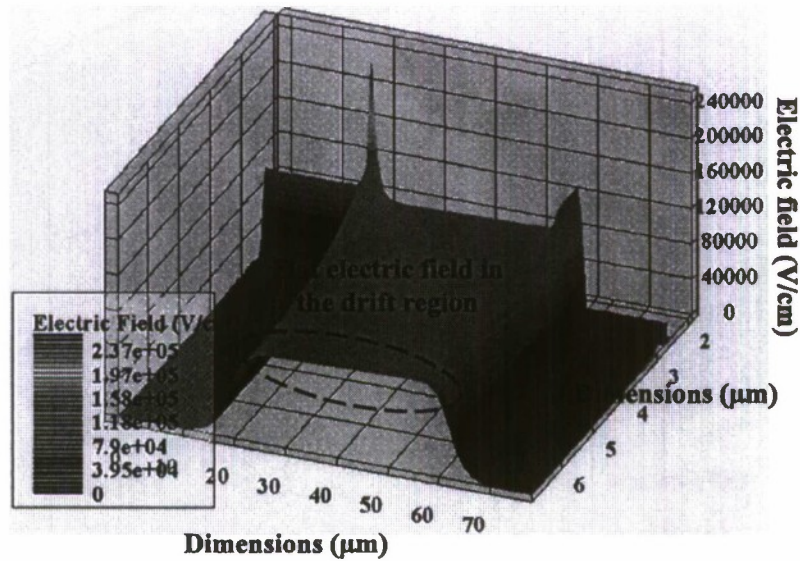


Fig. 7: Three-dimensional view of electric field distribution inside OTPT at the instant of breakdown.

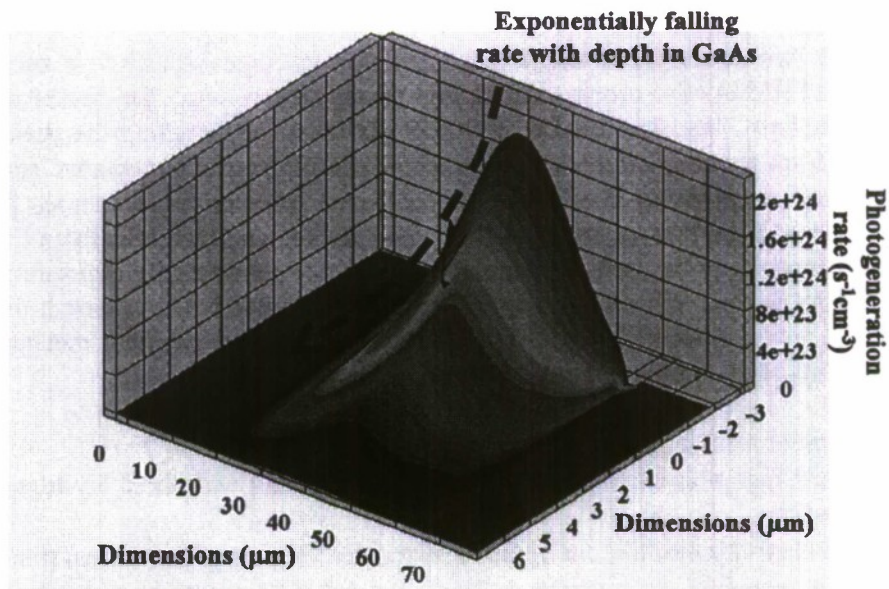
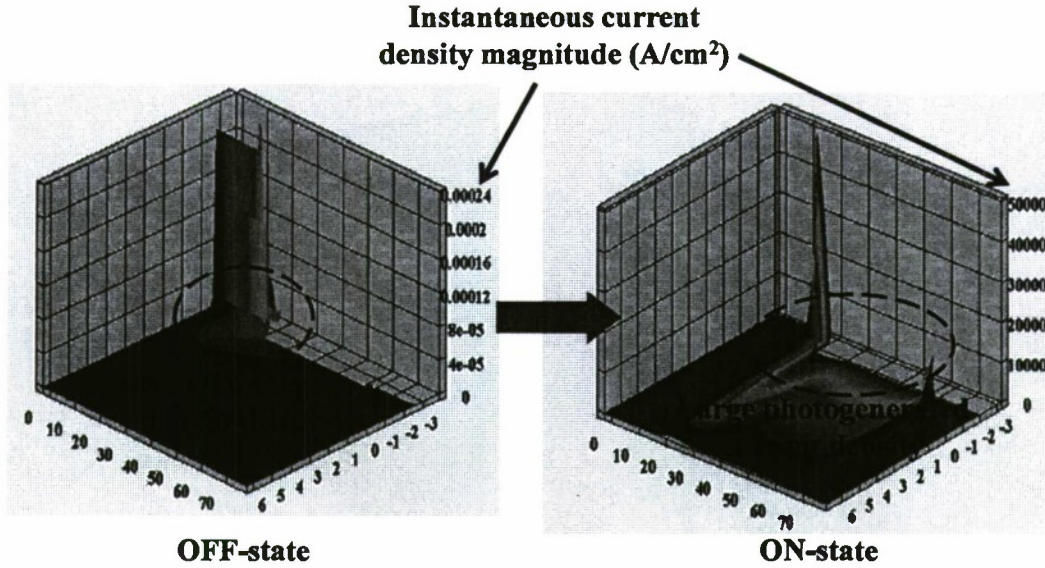


Fig. 8: Three-dimensional view of photogeneration rate inside OTPT.



**Fig. 9:** Transition of OTPT from OFF state to ON state when the device is illuminated by the triggering light source – multifold increase in the current density due to photogenerated electron-hole plasma injection into the base region of OTPT.

### 3.2. Numerical simulation framework and optical intensity modulation

Physics-based two-dimensional numerical simulator packages ATLAS is used for device simulation and ATHENA for process simulation (from Silvaco Inc.) for device modeling in a finite-element platform. We also use LUMINOUS platform for modeling the optical beam and MixedMode platform for coupled device-circuit simulation. Material parameters, such as lifetime, reflectivity, bandgap narrowing coefficient, are gathered from multiple sources [23, 24]. The overall framework and the flow of simulation exercise are shown schematically in Fig. 10

The physical models, to be used for simulation, can vary substantially depending on the type and material of the device. Whereas the optical-triggering device is GaAs based, the PSD could be silicon based power MOSFET or IGBT. Therefore, following physical mechanisms are all included in the integrated simulation environment,

- Photogeneration in direct bandgap material;
- Band-to-band recombination (for direct bandgap material) and Shockley-Read-Hall (SRH) recombination;
- Bipolar conductivity modulation in the base and drift region of the optical transistors;
- Metal-oxide-semiconductor interface effects for the PSD e.g. transverse electric field and channel mobility degradation;
- Bandgap narrowing and carrier-carrier scattering effects due to high current density in PSD.

A comprehensive list of physical models (Source: ATLAS and ATHENA manuals) is provided in Table 2. This also includes the process simulation models such as ion implantation and diffusion.



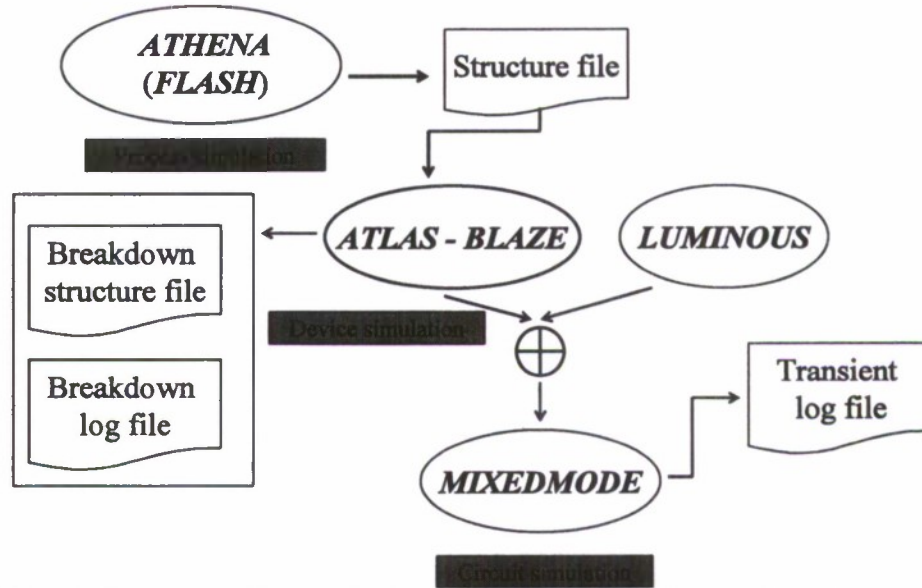


Fig. 10: Framework for physics based, two-dimensional numerical simulation.

Table 1: Major physical models of ATLAS-ATHENA platform used in numerical simulation.

Physical Models	Role in Simulation
full.cpl cluster.dam high.conc	Simulates the fully coupled ion implantation process that establishes a two-way coupling between the diffusions of dopants and point defects including cluster damage and high concentration effects.
BGN	Simulates the bandgap narrowing effect for large power devices.
ANALYTIC CCSMOB KLA	ANALYTIC simulates doping and temperature dependent mobility. CCSMOB simulates carrier-carrier scattering mobility effects. KLA or Klaassen's model is used for unified description of majority and minority carrier mobility including effects of lattice scattering, impurity scattering, and impurity clustering at high concentration.
CONSRH	Concentration and doping dependent SRH lifetime models.
IMPACT SELB	Selberrherr impact ionization model.
OPTR	Direct band-to-band recombination model in GaAs.
SURFMOB	Silicon-silicon dioxide surface scattering effects for MOS inversion channel mobility degradation.

Source: ATLAS user manual, Silvaco Inc.

Using the aforementioned simulation platform, the fundamental effects of optical parameter modulation have been studied for the GaAs OTPT. First, we show the dynamic time-evolution of



electric field inside OTPT when it is illuminated gradually from weaker to stronger optical intensity in Fig. 11. This change in the electric field pattern, from a 'potential barrier' to a 'potential downhill', facilitates the movement of bipolar carriers from high doped regions into the low-doped drift region and modulates the conductivity of OTPT. The gradual increment of the slope of the potential downhill can be observed from the plot, which establishes the basis behind the increasing conductivity of OTPT with higher optical intensity.

From Fig. 11 we observe a sign reversal of the slope in the electric field while going from dark to weak intensity condition and a large variation while going from weak to medium intensity condition. That implies OTPT starts conducting as soon as the optical signal is illuminated and undergoes a sharp change in the conductivity initially. However, while going from medium to strong intensity condition, we observe a relatively smaller change in the slope of the electric field which implies that above a certain intensity level, the conductivity variation will not be significant and it will enter a saturation regime.

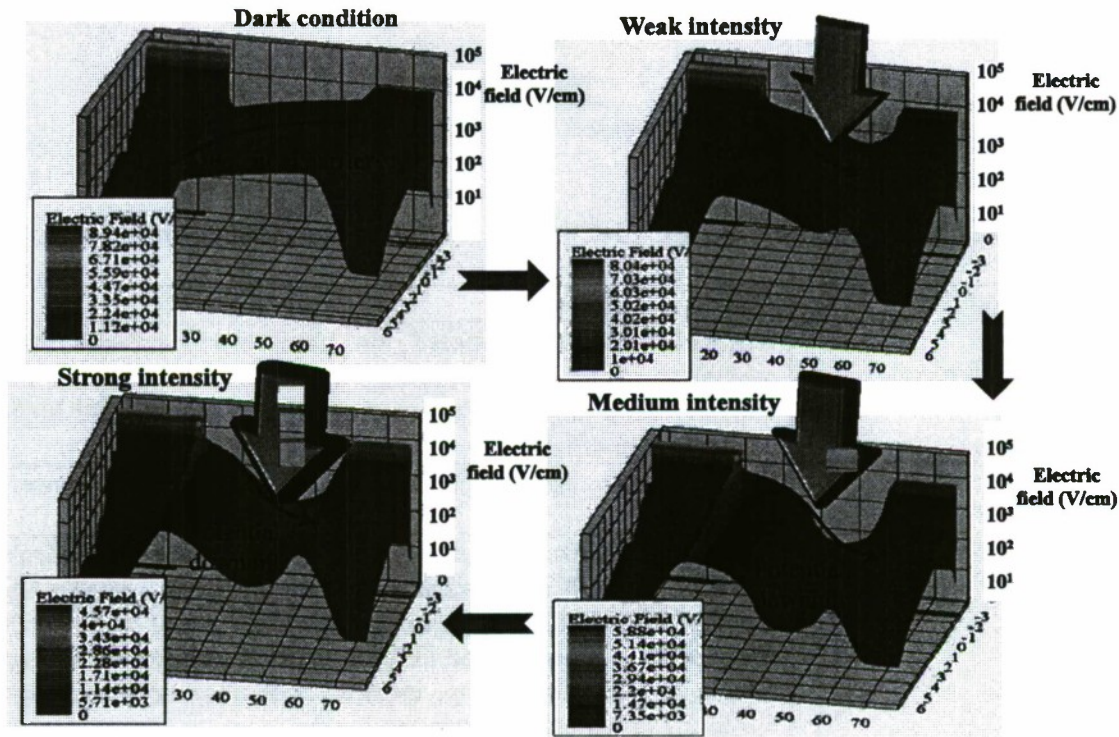


Fig. 11: Time-evolution of electric field inside OTPT during turn-on process – optical intensity increases in magnitude in consecutive frames.

### 3.3. Key design considerations

One critical design consideration is the thickness values for the P-body and  $N^+$  source layers. Although a thin P-body layer would increase the device gain, from the processing point of view the growth uniformity and dry etch controllability must be taken into consideration while designing the structure. Doping density of  $5 \times 10^{18} \text{ cm}^{-3}$  was targeted for the  $N^+$  source to ensure good ohmic contact. For the P-body layer,  $10^{17} \text{ cm}^{-3}$  doping density was based upon previous

design optimization data. Fig. 12a and 12b show that the device current undergoes minimal variation as the  $N^+$  source and P-body layer thicknesses are varied for these set of doping levels. However, the current level starts dropping slightly above  $0.8 \mu\text{m}$  P-body thickness. Also,  $0.75 \mu\text{m}$  was considered a safe lower limit for ensuring good etch controllability. Therefore,  $0.8 \mu\text{m}$  and  $0.5 \mu\text{m}$  were chosen as thickness for P-body and  $N^+$  source layer respectively to ensure good etch uniformity as well as high device gain.

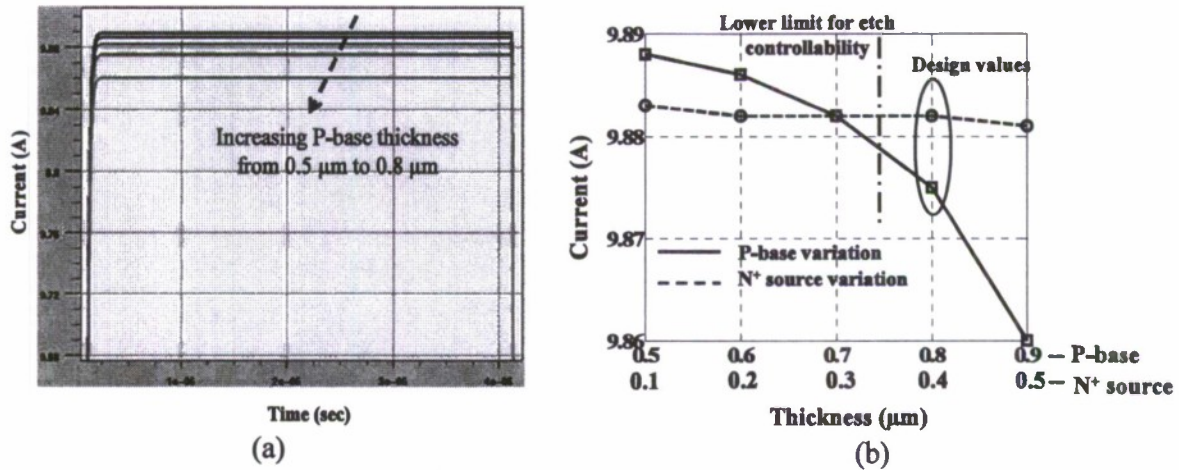


Fig. 12: (a) Switching simulation showing the peak current levels with varying P-body thickness and (b) parametric plot showing the variation of peak current with both P-body and  $N^+$  source thickness variation and the designed value.

Deposition of  $\text{SiN}_x$  anti-reflective coating is done by PECVD technique, where the thickness and refractive index of the deposited film may vary slightly depending on the process conditions such as pressure, temperature, gas flow rate etc. We calculate percent reflectivity as a function of varying AR coating thickness, for different refractive indices and plot the result in Fig. 13. Based on this result,  $300 \text{ nm}$  was chosen as the target thickness for the fabrication.

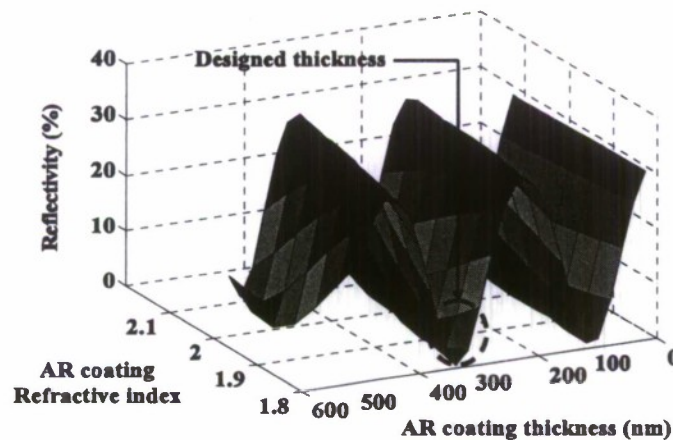


Fig. 13: Reflectivity as a function of  $\text{SiN}_x$  anti-reflective coating thickness and refractive index.

### 3.3. Photomasks for the fabrication of 2nd generation prototype

The photomask design for the 2<sup>nd</sup> generation prototype has been completed. The CAD drawings are shown in the following figures (Fig. 14 - Fig. 18). The process will consist of five major lithography steps for which five photomask layers are prepared.

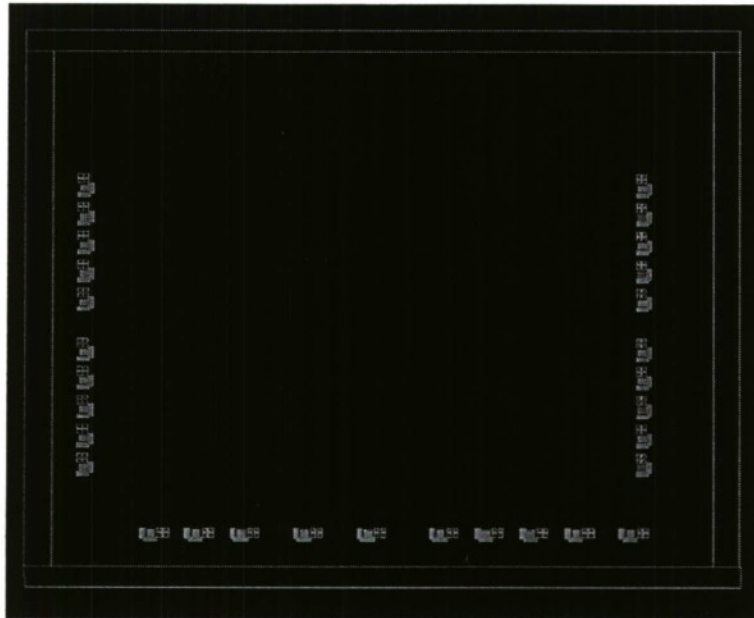


Fig. 14: Photomask for alignment marks (photomask\_0).

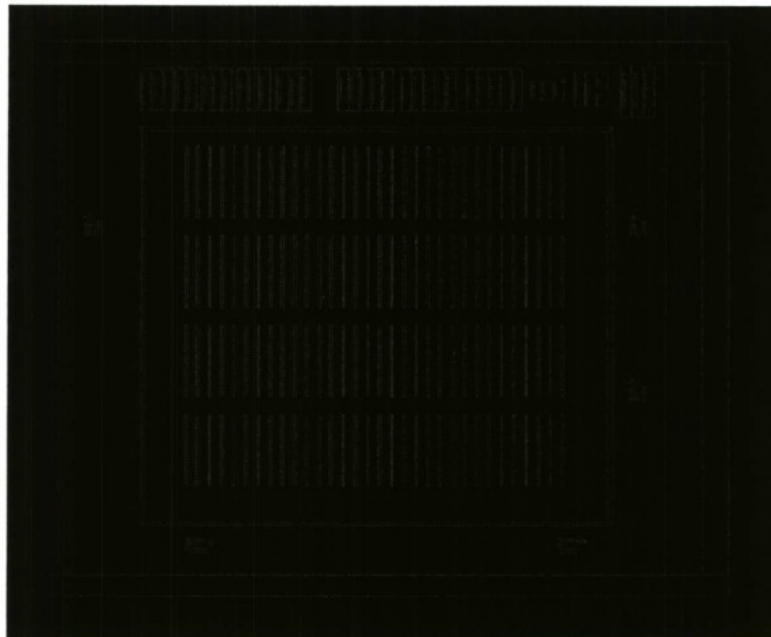
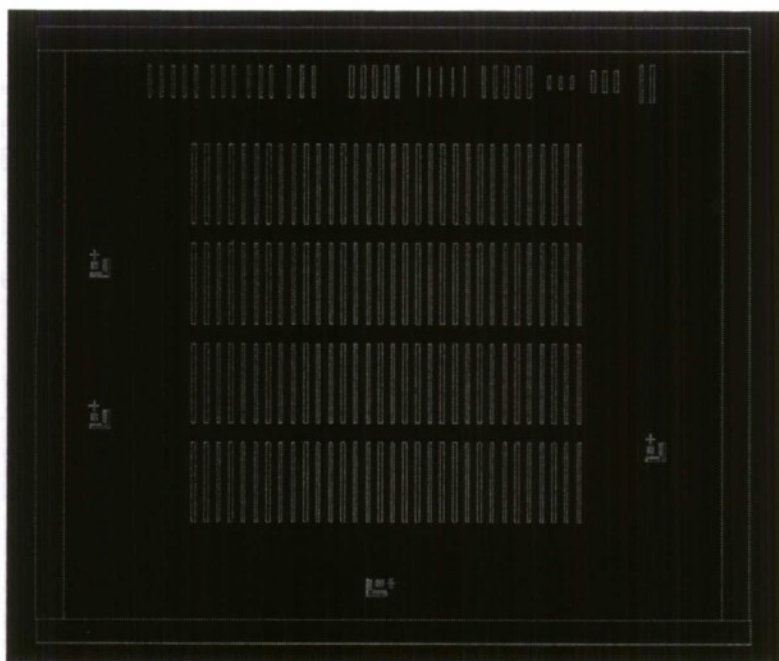
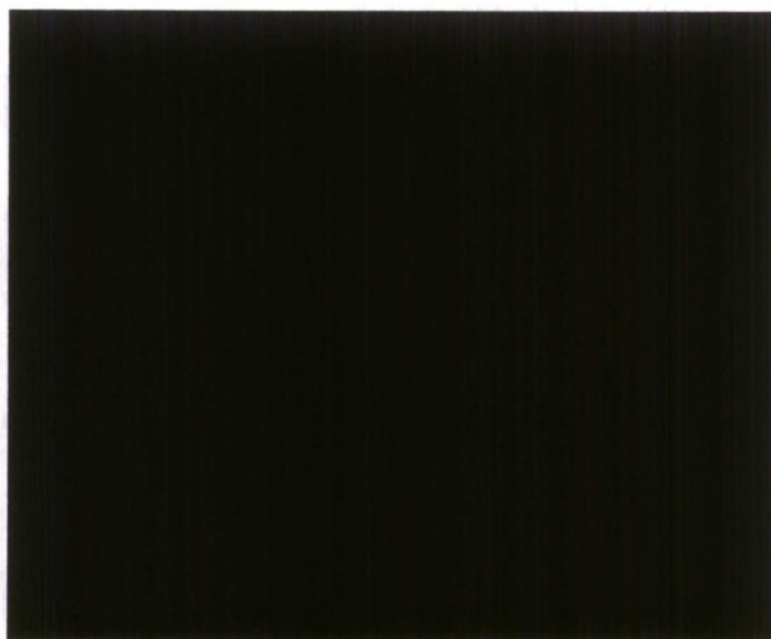


Fig. 15: Photomask for N<sup>+</sup> source patterning (photomask\_1).

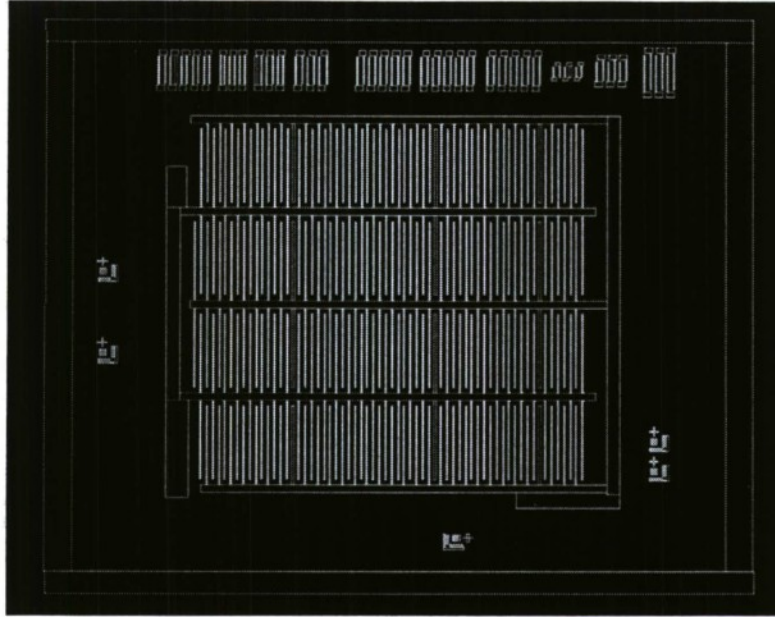




**Fig. 16:** Photomask for P-body patterning (photomask\_2).

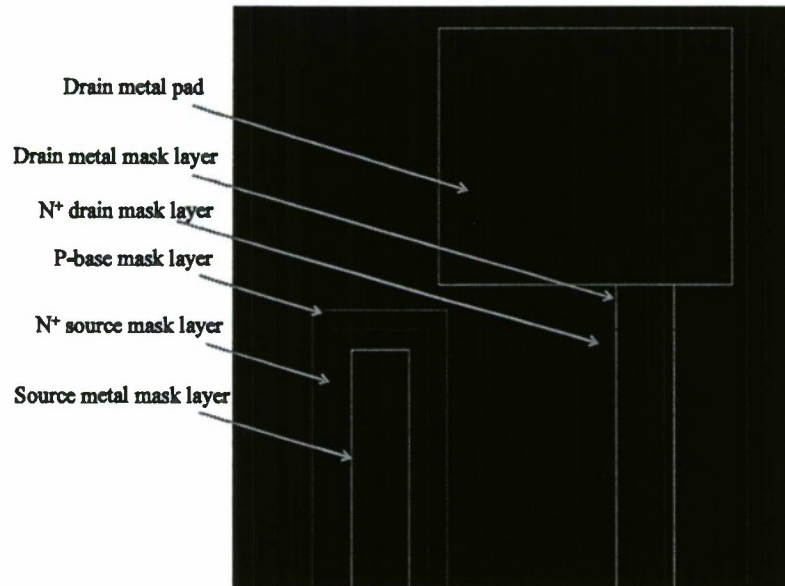


**Fig. 17:** Photomask for  $N^+$  drain patterning (photomask\_3).



**Fig. 18:** Photomask for metal deposition and patterning (photomask\_4).

In Fig. 19, we show the photomask picture of a single cell of the prototype device in close detail with all the layers visible. The source metal,  $N^+$  source and P-body rectangles are placed one within each other to prevent any low-impedance short-circuit path between drain and source through semi-insulating GaAs substrate. Except touching  $N^+$  source and  $N^+$  drain regions, metal elsewhere are placed on top of insulating  $SiN_x$  layer.



**Fig. 19:** A detailed close-up of the photomask for a single cell of the prototype device.

### 3.4. Low-doped epi growth for high voltage blocking

Although MOCVD growth of GaAs for moderate and high doping levels (in the  $10^{16} - 10^{18} \text{ cm}^{-3}$  range) is well-practiced and understood, controllably growing very low-doped epitaxial layers of moderate thickness (300 nm-1000 nm) is generally difficult to achieve due to background contamination. For optically-triggered power device, the high blocking voltage necessitates low doping density in the order of  $10^{13} - 10^{14} \text{ cm}^{-3}$ . The growth recipe was suitably adjusted and background contamination (carbon particulates etc.) was kept under control to achieve the desired level of doping. The doping density for calibration layers were measured by Hall-effect mobility technique. Apart from low doping density, high electron mobility was achieved for the N-drift layer which could help in reducing on-state resistance of the prototype. The calibration results are shown in Fig. 20.

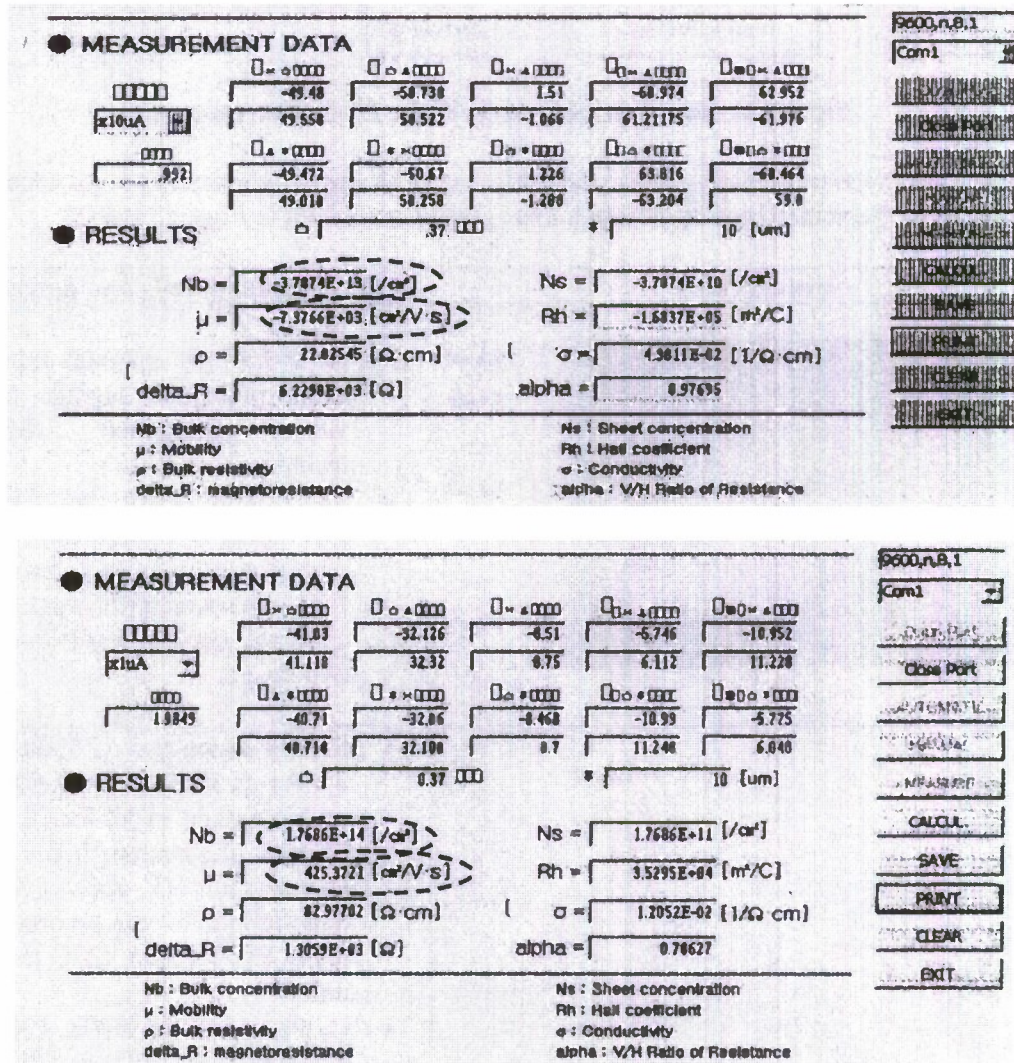


Fig. 20: Hall-measurements results (doping density and mobility) for epitaxial growth. Values are indicated by dotted ellipse.



### 3.5. Process-flow for the fabrication of 2<sup>nd</sup> generation prototype

The process-flow schematic for the fabrication of the 2<sup>nd</sup> generation prototype device is shown in Fig. 21. Overall process consists of 8 major steps including epitaxial growth, dry GaAs etching, high dose ion implantation and activation, passivation and anti-reflective layer deposition and metallization.

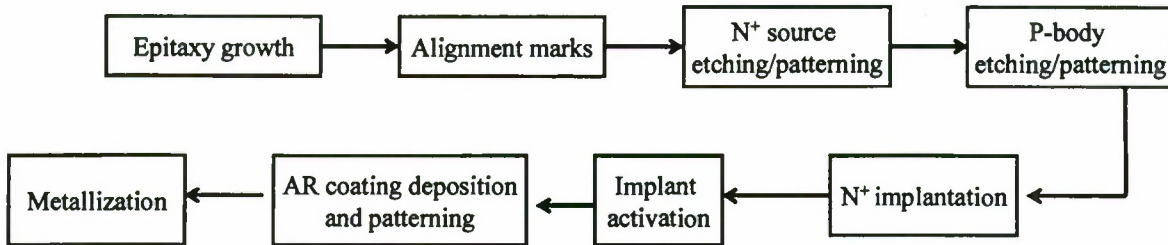

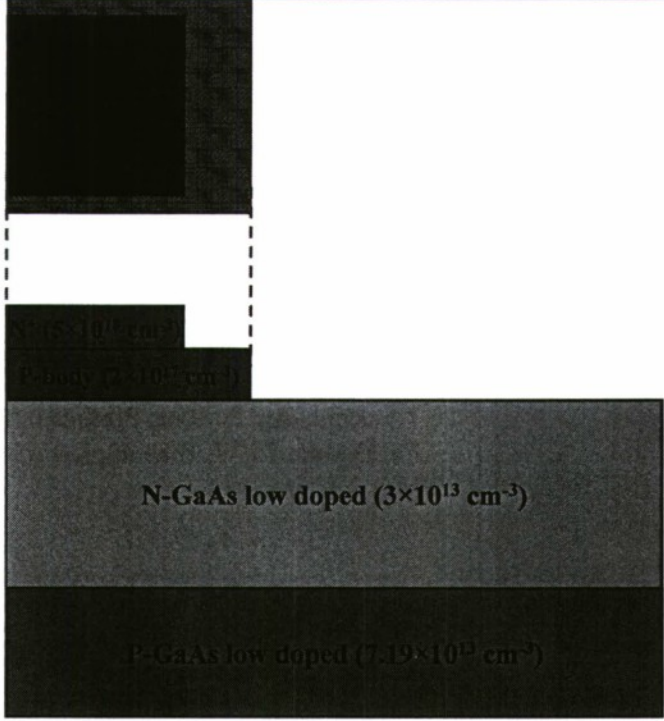


Fig. 21: A flow-chart schematic of the fabrication process.

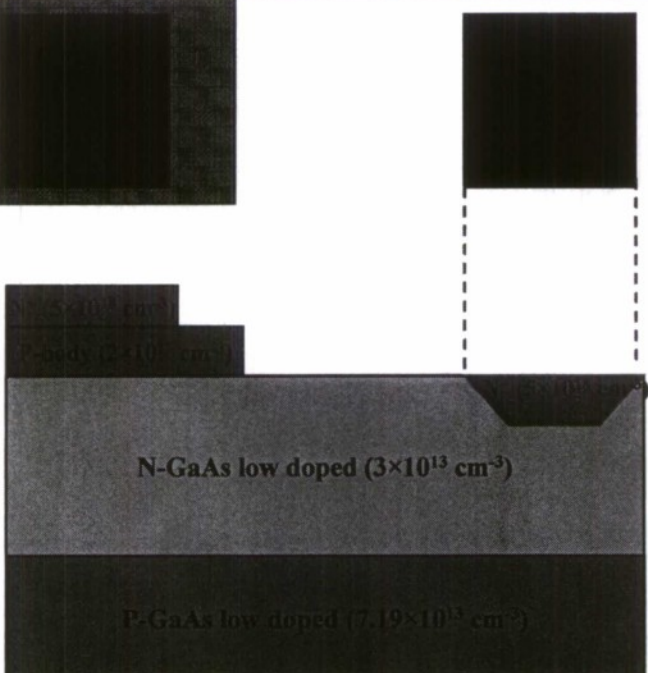
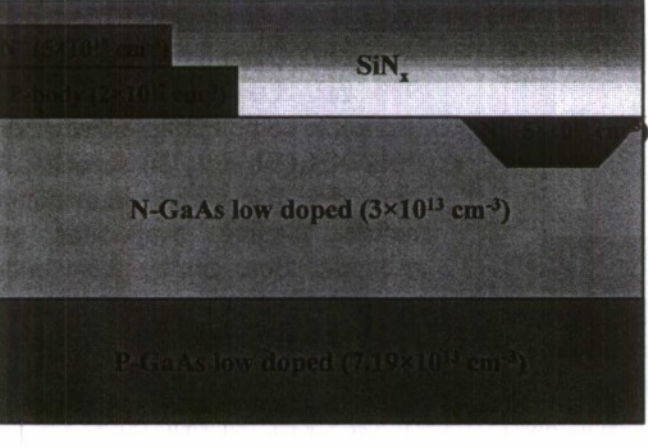
Detailed description of each process and relevant processing parameters are provided in the following table. Fabricated prototypes and micrographs are shown in Figs. 22 and 23.

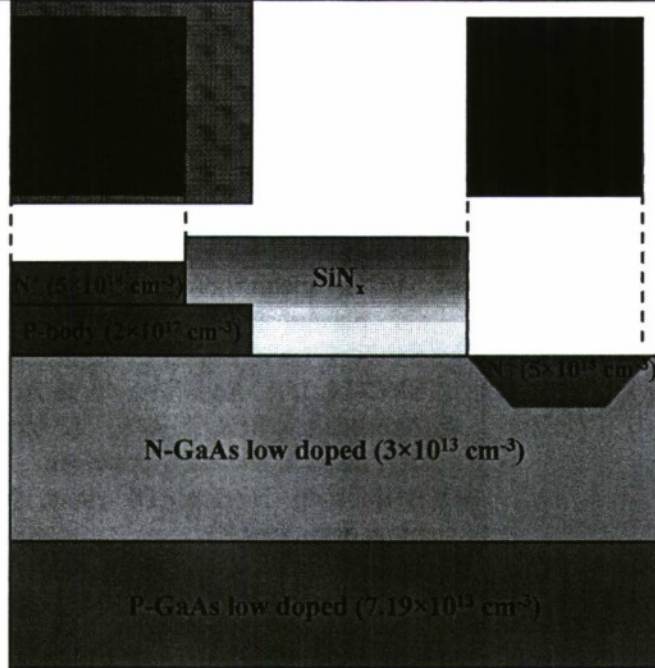
Process step	Processing details and description
	<ul style="list-style-type: none"> <li>Growth of the epitaxial structure by using molecular organic chemical vapor deposition (MOCVD) technique.</li> <li>The doping density for the bottom two layers were measured by Hall-mobility technique whereas Polaron C-V measurement was used to calibrate doping level for the top two layers.</li> </ul>
	<ul style="list-style-type: none"> <li>HMDS prime and AZ4330 resist on wafers at 3000 rpm for 60 s. Bake on hotplate at 110C for 60 seconds. Expose <b>photomask_0</b> for 120 mJ, Develop in 1:3 400K pre-mix to completion. (~ 60 seconds). Bake resist on Hotplate 120C bake for 1 min.</li> <li>O<sub>2</sub> Plasma: 50C, PWR: 1200 watts, MFC 5000 mV, 60 seconds.</li> </ul>
	<ul style="list-style-type: none"> <li>Patterning for the N+ source layer by dry reactive ion etching (RIE) of</li> </ul>

	<p>GaAs using photomask_1.</p> <ul style="list-style-type: none"> <li>• Vapor prime and AZ4330 resist on wafers at 3000 rpm for 60 s. Bake on hotplate for 60 seconds at 110C. Expose mask: <b>photomask_1</b> for 120 mJ. Develop in 1:3 400K premix to completion. ~60 seconds; post bake 1 minute at 120C on hotplate; O<sub>2</sub> Plasma cleaning at 50C, 1200 watts, MFC 5000 mV, for 60 seconds.</li> <li>• Etching setting - BCl<sub>3</sub>: 8 sccm, Cl<sub>2</sub>: 1.5 sccm, Ar: 2 sccm, Pressure: 0.5 Pa, Power: 75 W, Bias approx -540 V.</li> </ul>
	<ul style="list-style-type: none"> <li>• Clean in 2 acetone, 2 methanol, IPA and N<sub>2</sub> blow dry.</li> <li>• Step height measurement (3 locations).</li> </ul>
	<ul style="list-style-type: none"> <li>• Patterning for the N+ source layer by dry reactive ion etching (RIE) of GaAs using photomask_1.</li> <li>• Vapor prime and AZ4330 resist on wafers at 3000 rpm for 60 s. Bake on hotplate for 60 seconds at 110C. Expose mask: <b>photomask_2</b> for 120 mJ. Develop in 1:3 400K premix to completion. ~60 seconds; post bake 1 minute at 120C on hotplate; O<sub>2</sub> Plasma cleaning at 50C, 1200 watts, MFC 5000 mV, for 60 seconds.</li> <li>• Etching setting - BCl<sub>3</sub>: 8 sccm, Cl<sub>2</sub>: 1.5 sccm, Ar: 2 sccm, Pressure: 0.5 Pa, Power: 75 W, Bias approx -540 V.</li> </ul>

 <p>N+ (<math>5 \times 10^{18} \text{ cm}^{-3}</math>)</p> <p>P-body (<math>2 \times 10^{17} \text{ cm}^{-3}</math>)</p> <p>N-GaAs low doped (<math>3 \times 10^{13} \text{ cm}^{-3}</math>)</p> <p>P-GaAs low doped (<math>7.19 \times 10^{13} \text{ cm}^{-3}</math>)</p>	
	<ul style="list-style-type: none"> <li>• Clean in 2 acetone, 2 methanol, IPA and N<sub>2</sub> blow dry.</li> <li>• Step height measurement (3 locations).</li> </ul>
	<ul style="list-style-type: none"> <li>• 10% NH<sub>4</sub>OH etch, 30 seconds &amp; N<sub>2</sub> blow dry.</li> <li>• Silicon nitride deposition as the implant mask: NH<sub>3</sub>: 12 sccm SiH<sub>4</sub>: 400 sccm, HF/LF time: 17/3; target thickness 200 nm.</li> <li>• Vapor prime and AZ4330 resist on wafers at 3000 rpm for 60 s. Bake on hotplate for 60 seconds at 110C. Expose mask: <b>photomask_3</b> for 120 mJ. Develop in 1:3 400K premix to completion. ~60 seconds; post bake 1 minute at 120C on hotplate; O<sub>2</sub> Plasma cleaning at 50C, 1200 watts, MFC 5000 mV, for 60 seconds.</li> <li>• Silicon nitride dry etch; CF<sub>4</sub>O<sub>2</sub> at 33 % Pressure ~240 m torr, Power:</li> </ul>

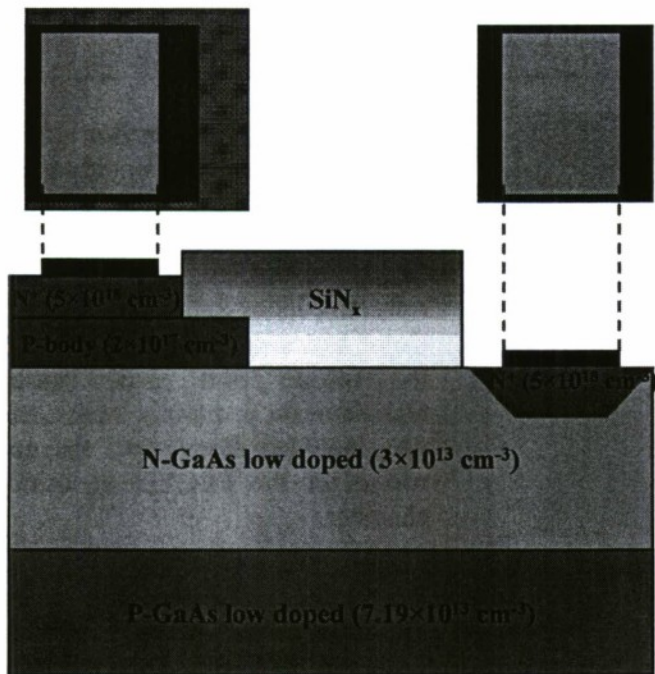


 <p>Si <math>5 \times 10^{14} \text{ cm}^{-2}</math> SiO<sub>2</sub> <math>2 \times 10^{13} \text{ cm}^{-2}</math> N-GaAs low doped (<math>3 \times 10^{13} \text{ cm}^{-3}</math>) P-GaAs low doped (<math>7.19 \times 10^{13} \text{ cm}^{-3}</math>)</p>	<p>300W.</p> <ul style="list-style-type: none"> <li>• 10% NH<sub>4</sub>OH etch, 30 seconds &amp; N<sub>2</sub> blow dry.</li> <li>• Si implant; <math>5 \times 10^{14} \text{ cm}^{-2}</math>, 50 keV.</li> <li>• O<sub>2</sub> Plasma: 50C, PWR: 1200 watts, MFC 5000 mV, 60 seconds.</li> <li>• Clean in 2 acetone, 2 methanol, IPA and N<sub>2</sub> blow dry.</li> <li>• SVC-14 clean, heat to 75-80C, ash O<sub>2</sub> plasma clean, 30 minutes in SVC-14, go to beaker of room temp SVC-14, IPA, Ace, Spray with Ace, Ace beaker, MeOH, IPA, N<sub>2</sub> blow dry, inspect. Repeat if not clean.</li> <li>• BHF strip Nitride. DI rinse, N<sub>2</sub> blow dry.</li> <li>• Arsine over pressure anneal in MOCVD chamber 850°C for 5 min.</li> </ul>
	<ul style="list-style-type: none"> <li>• 10% NH<sub>4</sub>OH etch, 30 seconds &amp; N<sub>2</sub> blow dry immediately prior to loading the wafers into the PECVD chamber.</li> </ul>
 <p>SiN <math>1.5 \times 10^{14} \text{ cm}^{-2}</math> SiO<sub>2</sub> <math>2 \times 10^{13} \text{ cm}^{-2}</math> N-GaAs low doped (<math>3 \times 10^{13} \text{ cm}^{-3}</math>) P-GaAs low doped (<math>7.19 \times 10^{13} \text{ cm}^{-3}</math>)</p>	<ul style="list-style-type: none"> <li>• Silicon nitride deposition using plasma-enhanced chemical vapor deposition (PECVD); NH<sub>3</sub>: 12 sccm SiH<sub>4</sub>: 400 sccm, HF/LF time: 17/3; target thickness 300 nm and refractive index 2.0.</li> <li>• Color and uniformity inspection of the nitride film using optical technique on a dummy wafer, that was included along with the epi-wafers in the PECVD deposition chamber.</li> </ul>
	<ul style="list-style-type: none"> <li>• Vapor prime and AZ4330 resist on wafers at 3000 rpm for 60 s. Bake on hotplate for 60 seconds at 110C. Expose mask: <b>photomask_1</b> for 120 mJ. Expose mask: <b>photomask_3</b> for 120 mJ. Develop</li> </ul>



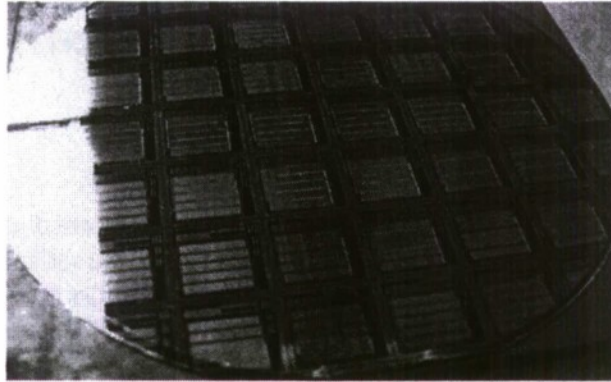
in 1:3 400K premix to completion. ~60 seconds; post bake 1 minute at 120C on hotplate;

- O<sub>2</sub> Plasma cleaning at 50C, 1200 watts, MFC 5000 mV, for 60 seconds.
- Silicon nitride dry etch; CF<sub>4</sub>O<sub>2</sub> at 33 % Pressure ~240 m torr, Power: 300W.
- Clean in 2 acetone, 2 methanol, IPA and N<sub>2</sub> blow dry.

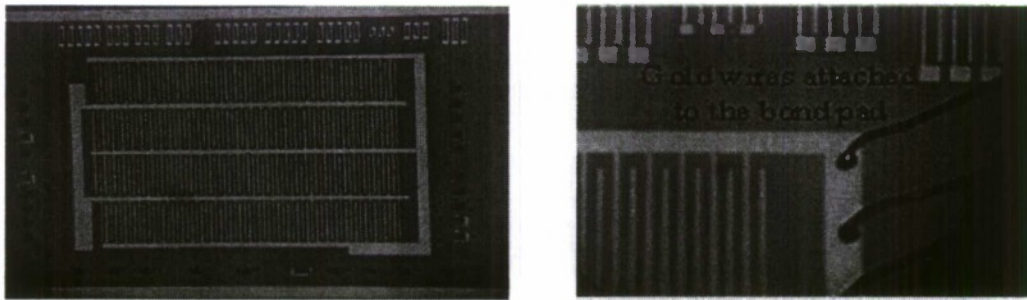


- Vapor prime and AZ4330 resist on wafers at 3000 rpm for 60 s. Bake on hotplate for 60 seconds at 110C. Expose clear field mask: **photomask\_4** for 140 mJ. Ammonia Oven bake, flood expose 900 mJ. Develop in 1:3 400K premix to completion, ~60 seconds.
- 10% NH<sub>4</sub>OH etch, 30 seconds, N<sub>2</sub> blow dry. Dip wafers immediately before loading evaporator and minimize time getting them under vacuum after etching native oxide.
- Au: 140Å, 3Å/s, Ge: 140Å 3Å/s, Au: 140Å, 3Å/s, Ni: 100Å 3Å/s, Au: 5,000 Å, 8Å/s.
- Lift-off in acetone, rinse in acetone, methanol, IPA, DI water and N<sub>2</sub> blow dry.
- Alloy: 370C RTP 30 seconds. Ramp to 370C in 180 seconds, hold 30 seconds, natural cool 240 seconds.





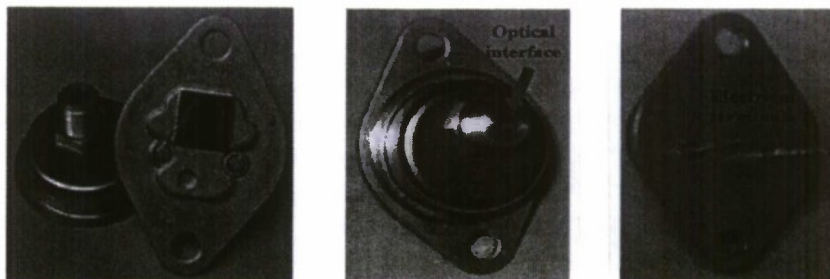
**Fig. 22:** Fabricated 3" wafer with OTPT devices.



**Fig. 23 (a)** Micrograph of the fabricated OTPT prototype, wire bonding

### ***3.6 Packaging details for the prototype***

For the switching test, the prototype device was packaged for fiber-coupling. Individual chip was diced from the wafer and bonded to a thermal pad (beryllium oxide) using silver epoxy at the bottom of a high heat load (HHL) laser-diode package. Gold wire bonding was attached to the electrical pads and to the external terminals. An optical window of pre-fixed dimension was etched out in the top lid of the package and the package is hermetically sealed in an inert gas atmosphere. The optical window dimension is made such as to accept a SMA-905 connector which is an industry-standard termination for optical fiber. Details are shown in Fig. 24.



**Fig. 24:** (a) GaAs OTPT die attached to the package floor (b) optical fiber coupling through SMA-905 port, and (c) electrical terminals at the backside



## 4. EXPERIMENTAL STUDIES ON OTPT AND OPTICAL INTENSITY MODULATION OF OTPT PARAMETERS

### 4.1 Optical source, driver, and fiber details

GaAs/AlGaAs based FAP600 laser (from Coherent Inc.) was used as the optical source (Fig. 25). This is a 24 Watts (CW rated), 808 nm laser with spherically homogenized output terminated in a multi-mode fiber bundle with SMA-905 connectors on both ends (Fig. 25). PCX-7410 laser driver module (from Directed Energy) was used as the pulsating current source for energizing the laser. FAP600 laser also has an optical sampling port which delivers a fraction of actual output light for indication purpose. But, due to very fast switching times (rise and fall time of the laser drive, laser, and device were recorded in the order of few tens of nanoseconds) we measured the laser drive current directly from a current monitor output terminated in a 50 Ohm input of the oscilloscope. The optical fiber is a patch cable with multimode index fiber with silica core (featuring 800  $\mu\text{m}$  core diameter and 0.37 numerical aperture) and hard polymer cladding. It is surrounded by tefzel jacket for high temperature withstanding. Both ends are terminated in SMA-905 connector.

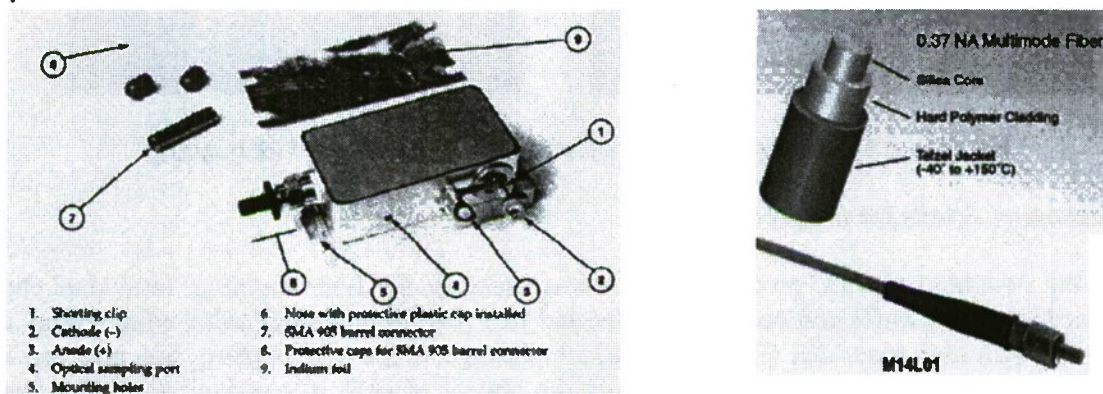


Fig. 25: Laser and optical fiber details.

### 4.2. Switching experimental setup

The switching test set-up consists of the laser driver, DC voltage bias supply, load resistor, device under test (DUT), and multi-channel oscilloscope. The arrangement is shown schematically in Fig. 26. The switching waveform is programmed into the laser driver that generates current pulses accordingly. A microstrip line connector is used to connect laser driver output to the laser diode terminals to reduce inductance and associated voltage spikes (otherwise fast changing current pulses may result in high voltage across laser diode terminals thereby potentially damaging it). The current driver output from the laser driver is monitored through an integrated front-end port. The equivalent voltage signal corresponding to a given current output is negative in magnitude e.g. for 20A current output, -1V voltage signal is produced at the current monitor output.

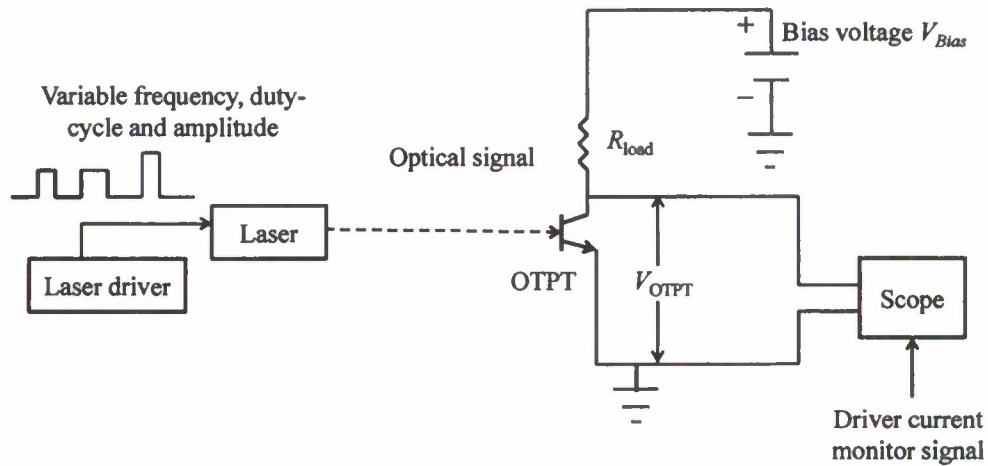


Fig. 26: Resistive load experimental characterization circuit for OTPT.

#### 4.3. Dark resistivity of OTPT

Dark resistivity of the fabricated OTPT prototype device is measured in non-illuminated condition using a Tektronix 371A curve tracer and the result is shown in Fig. 27. Less than  $1 \mu\text{A}$  current flows through OTPT when steady-state 50 V is applied across the device. Therefore, the dark resistance can be calculated as  $\approx 50 \text{ V}/1 \mu\text{A} = 50 \text{ M}\Omega$ .

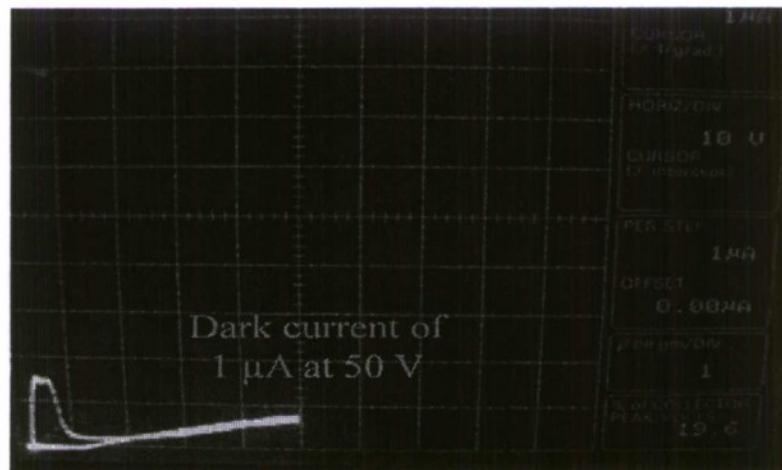
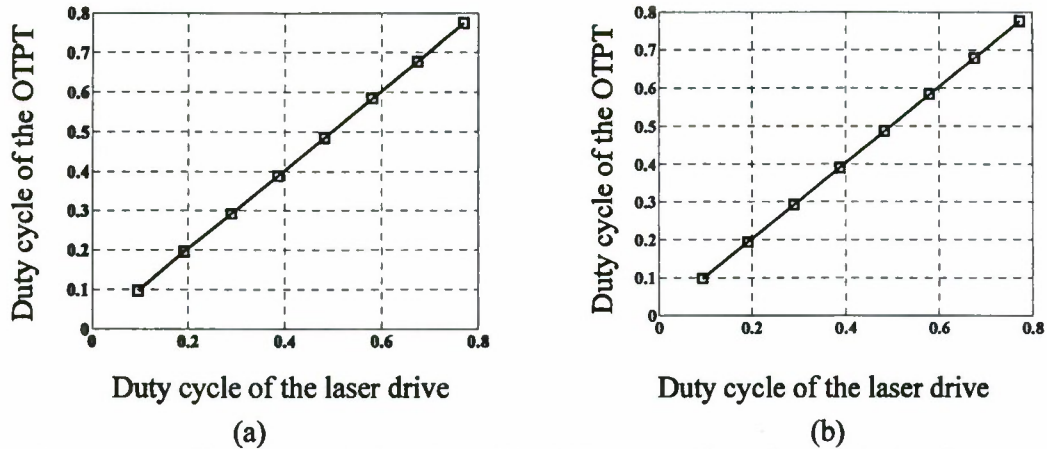


Fig. 27: Forward conduction characteristic of OTPT without illumination – dark resistance of  $> 50 \text{ M}\Omega$  was measured.

#### 4.4. Nominal switching and pulse-following characterizations

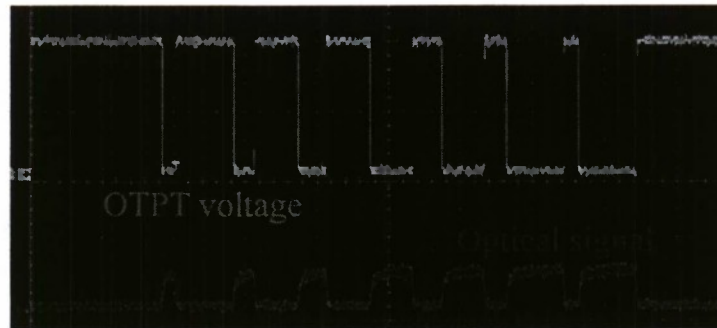
Thereafter, we characterize the single OTPT for nominal operation and measurement of its switching parameters. The resistive load circuit, used for simulation and benchmark experiment, is shown in Fig. 26. One of the most important characteristic to be measured is the ability of

OTPT to follow optical triggering signal of variable pulse-width and frequency. We measure OTPT duty cycle by varying the laser drive signal (equivalently optical triggering signal) duty cycle over a broad range for two different frequencies and show the linear relationship (Fig. 28).



**Fig. 28:** Experimentally measured linearity of OTPT duty cycle and optical signal over a wide range of duty cycles (0.1-0.8) for two different frequencies – (a) 20 kHz and (b) 80 kHz.  $V_{\text{bias}} = 60 \text{ V}$ ,  $R_{\text{ext}} = 1000 \Omega$ ,  $P_{\text{opt}} = 1 \text{ Watt}$ .

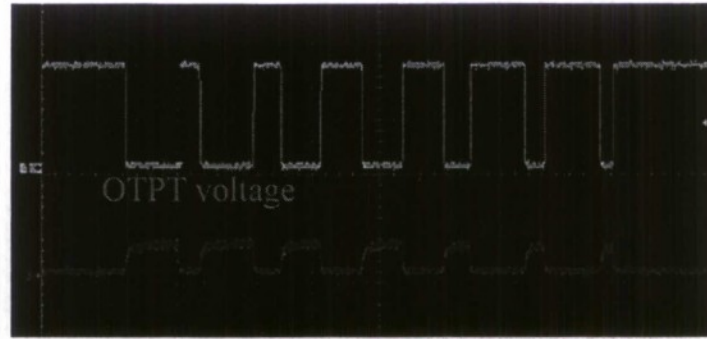
Although previous results demonstrate that OTPT closely follows optical signal over a wide range of duty cycle, these tests are performed at fixed value of duty cycle. For a number of power electronics topologies (pulse-width modulated converters), a continuously varying duty cycle operation is common. In Fig. 29, such a switching operation is shown where OTPT tracks continuously varying optical signals both for increasing and decreasing pulse-widths.



**Gradually increasing duty cycle**

(a)





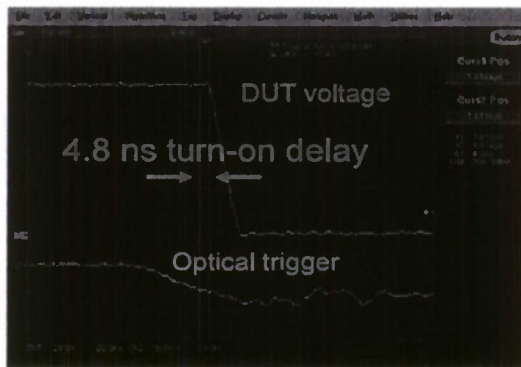
Gradually decreasing duty cycle

(b)

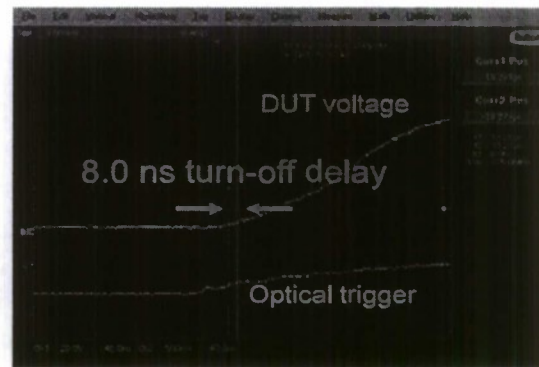
**Fig. 29** Switching operation for continuously varying duty cycle (i.e. pulse-width modulation). Vertical axis – 10 V/div (for OTPT voltage), horizontal axis – 10 ms/div.  $V_{\text{bias}} = 20$  V,  $R_{\text{ext}} = 100$   $\Omega$ ,  $P_{\text{opt}} = 1$  Watt.

#### 4.5. Turn-on and turn-off dynamics characterizations

Next, in Figs. 30 and 31 we show the turn-on and turn-off dynamics of OTPT. Turn-on and turn-off delays are measured as the difference between the time instants where the laser drive signal crosses the threshold level (i.e. the optical signal initiation instant) and the initiation of change in OTPT voltage (starts falling during turn-on and starts rising during turn-off). Rise and fall times are defined as the time taken to change the voltage across OTPT from 10% to 90% (or vice versa) to its steady-state value. Low turn-on and turn-off delay and fast rise time are demonstrated. Experimental conditions are:  $V_{\text{bias}} = 80$  V,  $R_{\text{ext}} = 1000$   $\Omega$ , frequency – 50 kHz, duty cycle – 50%,  $P_{\text{opt}} = 1$  Watt.



(a)



(b)

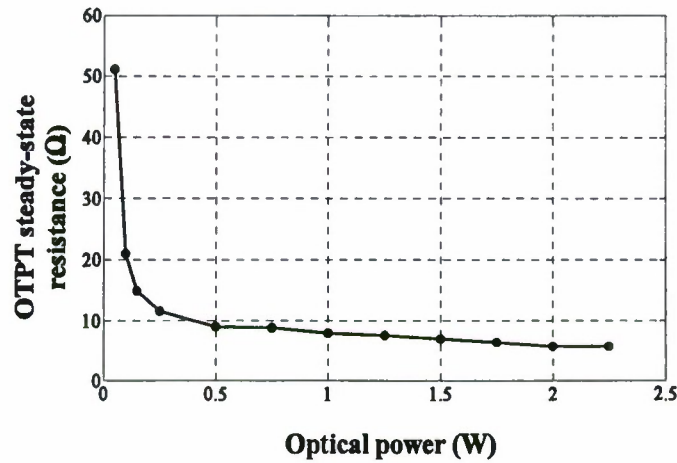
**Fig. 30:** Experimental waveforms – (a) turn-on and (b) turn-off delay of OTPT. Scale - vertical axis: 20 V/div, horizontal axis: (a) 20 ns/div, (b) 40 ns/div.  $V_{\text{bias}} = 80$  V,  $R_{\text{ext}} = 1000$   $\Omega$ , frequency – 50 kHz, duty cycle – 50%,  $P_{\text{opt}} = 1$  Watt.



**Fig. 31:** Experimental waveforms – (a) rise time and (b) fall time of OTPT. Scale - vertical axis: 20 V/div, horizontal axis: (a) 20 ns/div, (b) 400 ns/div.  $V_{\text{bias}} = 80$  V,  $R_{\text{ext}} = 1000 \Omega$ , frequency – 50 kHz, duty cycle – 50%,  $P_{\text{opt}} = 1$  Watt.

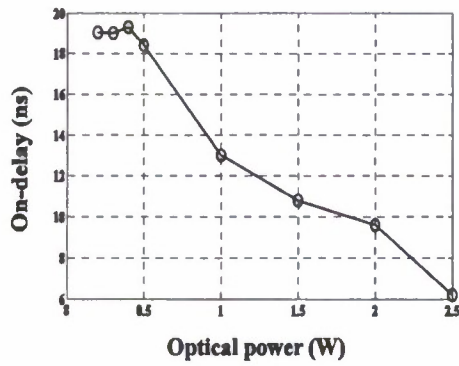
#### 4.5. Optical intensity modulation of OTPT parameters

The optical modulation of PSD switching dynamics depends on the optical modulation of OTPT on-state resistance (or conductivity). We measure the small-signal resistance modulation by point-by-point method. The forward drop of the OTPT during steady-state conduction ( $V_{\text{OTPT}}$  as per Fig. 26) is measured for different laser drive currents (corresponding to different optical power levels) and the results are parametrically plotted (Fig. 32) [25] to show the variation of steady-state conductivity with optical power.

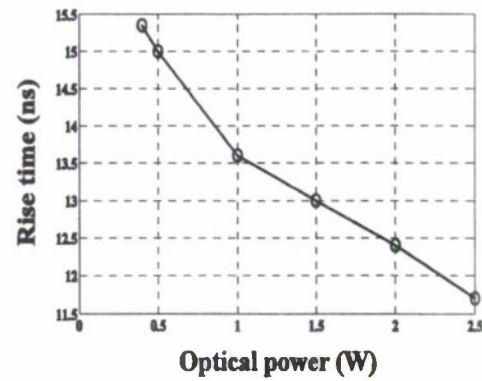


**Fig. 32:** Experimentally measured modulation of OTPT steady-state on-resistance with varying optical power.  $V_{\text{Bias}} = 10$  V,  $R_{\text{load}} = 50 \Omega$ , frequency = 5 kHz, duty cycle = 50%.

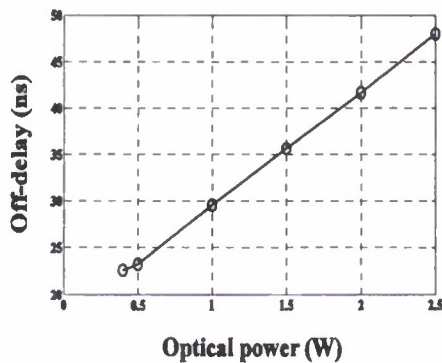
Next, in Fig. 33, we show the variation in the turn-on and turn-off dynamics of OTPT. Turn-on and turn-off delays are measured as the difference between the time instants of the initiation of laser drive signal and the initiation of change in OTPT voltage (starts falling during turn-on and starts rising during turn-off). Rise and fall times are defined as the time taken to change the voltage across OTPT from 10% to 90% (or vice versa) to its steady-state value.



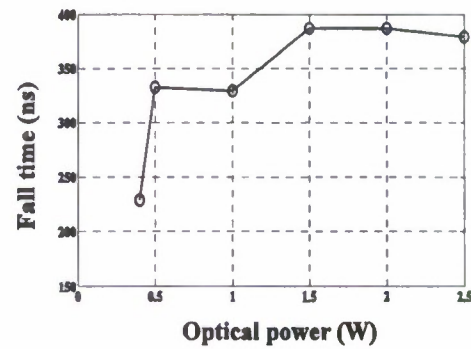
(a)



(b)

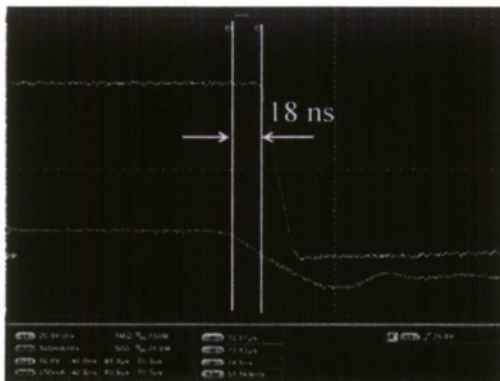


(c)

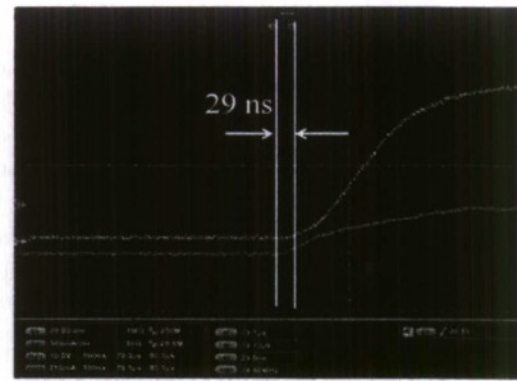


(d)

**Fig. 33:** Parametric result – experimentally measured (a) turn-on delay, (b) rise time, (c) turn-off delay, and (d) fall time with varying optical power.  $V_{\text{bias}} = 60$  V,  $R_{\text{ext}} = 1000 \Omega$ , frequency – 50 kHz, duty cycle – 50%.



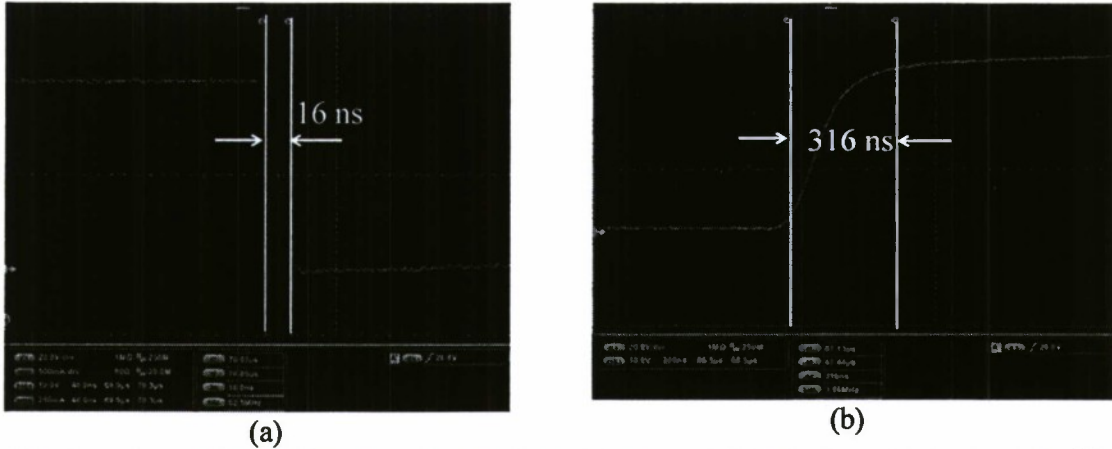
(a)



(b)

**Fig. 34:** Experimental waveforms – (a) turn-on delay (18 ns) and (b) turn-off delay (29 ns) of OTPT. Scale - vertical axis: 10 V/div, horizontal axis: (a) 40 ns/div, (b) 100 ns/div.  $V_{\text{bias}} = 60$  V,  $R_{\text{ext}} = 1000 \Omega$ , frequency – 50 kHz, duty cycle – 50%,  $P_{\text{opt}} = 0.5$  Watt.





**Fig. 35:** Experimental waveforms – (a) rise time (16 ns) and (b) fall time (316 ns) of OTPT. Scale - vertical axis: 10 V/div, horizontal axis: (a) 20 ns/div, (b) 200 ns/div.  $V_{bias} = 60$  V,  $R_{ext} = 1000 \Omega$ , frequency – 50 kHz, duty cycle – 50%,  $P_{opt} = 0.5$  Watt.

## 5. EXPERIMENTAL STUDIES ON HYBRID OTPT-PSD AND OPTICAL INTENSITY MODULATION OF PSD SWITCHING DYNAMICS

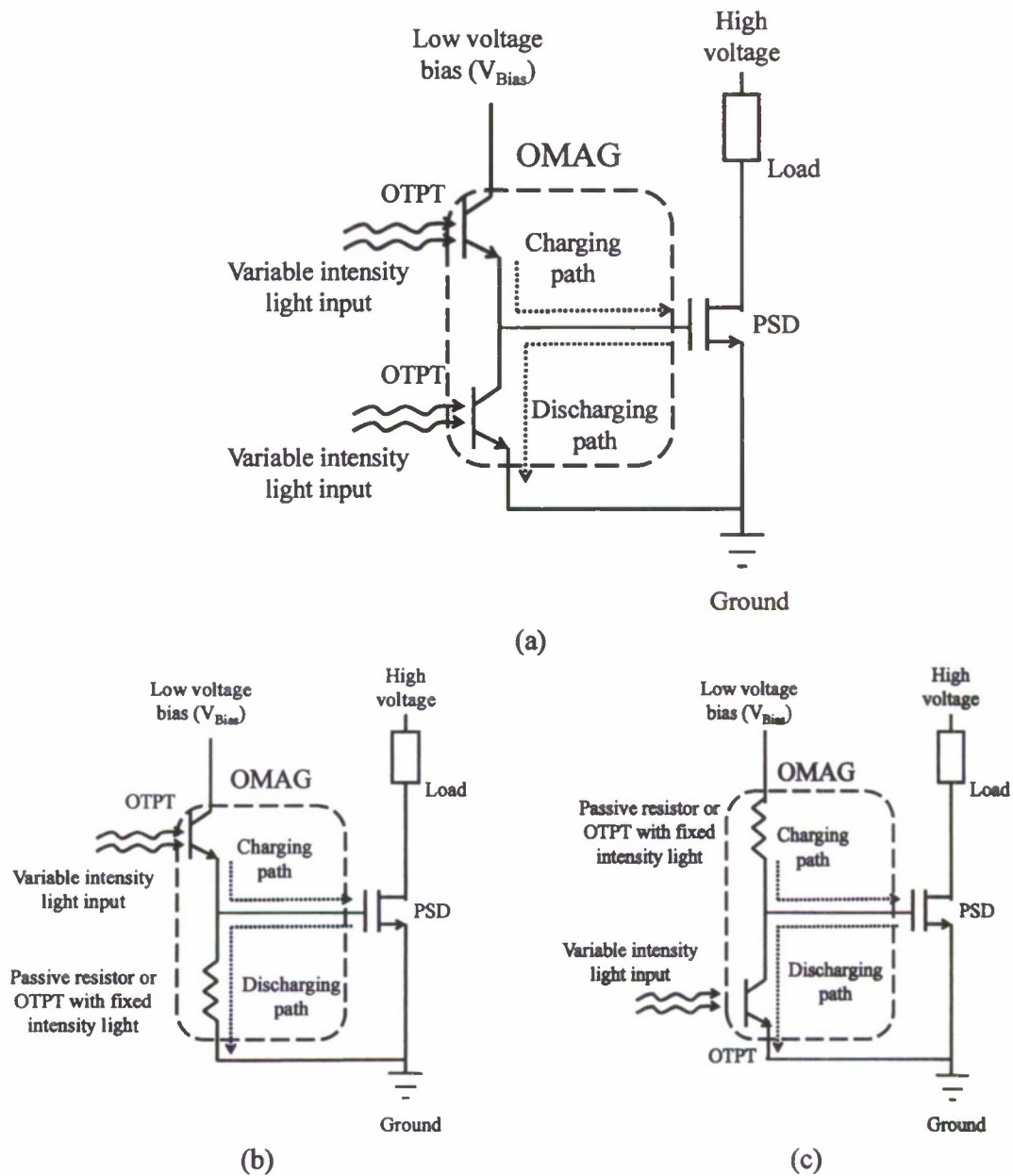
After characterizing single OTPT, we discuss about the switching dynamics modulation when OTPT is coupled to power semiconductor device (PSD). Theoretical basis of optical intensity modulated switching dynamics variation of PSD is discussed with a case illustration for a power MOSFET as PSD. Experimental validation is demonstrated by coupling OTPT with a power MOSFET and characterizing the switching performance with varying optical power.

### 5.1. *Optically-modulated Active Gate Control (OMAG) architecture for full controllability of turn-on and turn-off dynamics of PSD*

The structural concept of the OMAG [25] is illustrated in Figs. 36a - 36c. It is noted here that, other variations of OMAG structures are feasible and have been developed in our laboratory as well. In either of the schemes, the main idea is to control the excitation current for triggering the PSD (and hence control its switching dynamics) by modulating the photonic excitation of one or more OTPT devices.

The PSD gate is connected to the collector/emitter terminal of the OTPT and the PSD drain/collector (e.g. MOSFET/IGBT) is connected to a high-voltage power supply in series with a current-limiting load resistor. The source/emitter of the PSD is grounded and at the same reference point as that of the ground of the logic bias  $V_{Bias}$ . The PSD gate needs to be charged to the level of  $V_{Bias}$  to turn it on and to be discharged to the ground potential to turn it off. In the off-state (or non-illuminated state), the OTPT is in a non-conducting, high-resistivity mode. When light falls on the OTPT and the on-state is initiated, photogeneration and subsequent transistor action causes OTPT's conductivity to increase manifold. Essentially, OTPT acts as either the charging or discharging element for the PSD (when it is illuminated and in on state) depending on whether the OTPT is placed in the charging/discharging path.

In the first scheme (Fig. 36a), active control of both turn-on and turn-off dynamics of the PSD is realizable by exciting OTPT devices (placed in both the Charging as well as Discharging path)



**Fig. 36:** OMAG structural schematics with (a) full turn-on and turn-off controllability using two OTPTs, (b) turn-on controllability and passive turn-off using one OTPT in the charging path and a passive resistor (or an OTPT with fixed optical signal amplitude) in the discharging path, and (c) turn-off controllability and passive turn-on using one OTPT in the discharging path and a passive resistor (or an OTPT with fixed optical signal amplitude) in the charging path.

with variable amplitude of light. Further, since the turn-on and turn-off dynamics are controlled using two separate photonic excitation sources, the control rate of these switching dynamics can be different and as such associated device stresses and switching losses of the PSD, and the overall electromagnetic noise and emissions from the PSD based power electronics can be separately controlled as well. In the scheme of Fig. 36b, only turn-on dynamics is controllable (by employing OTPT with variable amplitude optical signal in the Charging path) whereas the turn-off dynamics of the PSD is determined by the Discharging-path resistance and the PSD device capacitance. The Discharging-path resistance can either be a physical passive resistive element or an OTPT with fixed amplitude optical signal (as OTPT with fixed optical trigger amplitude acts as a fixed resistor). Similarly, the scheme in Fig 2c demonstrates turn-off controllability by employing OTPT with variable amplitude optical signal in the Discharging path.

### 5.3. Relationship between PSD switching parameters and optical intensity

As the OTPT couples with different types of power devices in the optical-triggering structure, it opens up the possibility of various types of interactions between the optical-triggering structure and the PSD. We discuss the dynamic optical modulation concept by analyzing a case of where the PSD is a power MOSFET. According to Fig. 36a because OTPT is in series in the charging path of the power MOSFET gate, variation in optical power, which modulates the OTPT resistance (as seen from previous chapter) is expected to modulate the rise time of the power MOSFET which depends on the total resistance in the charging path. Denoting the on-resistance of charging path OTPT by  $R_{OTPT,on}$ , and using a resistive gate charging model, we can write down,

$$C_{iss} \frac{dv_{gs}}{dt} = \frac{V_{Bias} - v_{gs}}{R_{OTPT,on}} \quad (35)$$

$$\Rightarrow v_{gs}(t) = V_{Bias} \left( 1 - e^{-\frac{t}{R_{OTPT,on} C_{iss}}} \right)$$

where  $C_{iss}$  is the effective input capacitance of the MOSFET,  $v_{gs}$  is the gate-source voltage. MOSFET begins conducting when the  $v_{gs}$  reaches threshold voltage  $V_{Th}$ . Effectively the turn-on delay can be said to be equal to the sum of the rise time of the OTPT itself ( $t_{rise,OTPT}$ ) and the time needed for charging the input capacitance to the threshold level. Therefore we can deduce an expression for delay  $t_{delay,on}$  as,

$$t_{delay,on} = t_{rise,OTPT} + C_{iss} R_{OTPT,on} \ln \left( \frac{V_{Bias}}{V_{Bias} - V_{Th}} \right) \quad (36)$$

Therefore (36) illustrates that the turn-on delay could be controlled by varying the optical power. With increasing optical power, all other parameters being equal, (36) predicts a decrease in turn-on delay because the  $R_{OTPT,on}$  decreases with increasing optical power. Doing similar analyses, and following [26], rise time ( $t_r$ ), fall time ( $t_f$ ), and turn-off delay ( $t_{delay,off}$ ) can be expressed as follows,



$$t_r = C_{iss} R_{OTPT,on} \ln \left( \frac{V_{Bias}}{V_{Bias} - \left( V_{Th} + I_{in} / g_{fs} \right)} \right) \quad (37);$$

$$t_f = C_{iss} R_{OTPT,off} \ln \left( \frac{V_{Th} + I_{in} / g_{fs}}{V_{Th}} \right) \quad (38)$$

$$t_{delay,off} = t_{fall,OTPT} + C_{iss} R_{OTPT,off} \ln \left( \frac{V_{Bias}}{V_{Th}} \right) \quad (39)$$

We note that rise time and fall time depends on the  $R_{OTPT,on}$  and  $R_{OTPT,off}$  respectively which are functions of optical intensity (according to equation (14)) and hence should be controllable by optical power variation. With increasing optical power, all other parameters being equal, (37) indicates a decrease in rise time because the  $R_{OTPT}$  decreases with increasing optical power (as seen from Fig. 32). Similarly, fall time of the PSD depends on the on-resistance of the OTPT placed in the discharging path i.e.  $OTPT_{off}$ . Turn-off delay contains an additional term of the fall time of the OTPT itself.

#### 5.4. Experimental characterization of optical intensity modulation of switching dynamics

We vary the optical-triggering power and measure the switching performance of the PSD to demonstrate the optical modulation capability. The circuit arrangement is shown in Fig. 37 and the PSD is CoolMOS™ power MOSFET (part number 47N50) from Infineon. Time-domain snapshots of a specific switching event are shown in Fig. 40a-Fig. 40d. The parametric results, with variation in optical power, are shown in Fig. 38. As discussed earlier, rise time and turn-on delay decreases with the variation in on laser or with the simultaneous variation in on and off laser intensity whereas they do not get much affected by the variation in only off-laser. Similarly, fall time and turn-off delay decreases with the variation in off laser or with the simultaneous variation in on and off laser intensity whereas they do not get much affected by the sole variation in on-laser.

Due to the small time scale in the range of nanoseconds, it is necessary to estimate the range of error in recording switching dynamics data. In this regard, we did a random time sampling of the identical rise time waveform and record their values. The sampling distribution is illustrated in Fig. 39 which shows a maximum spread of 6 ns with almost equal peak positive and negative deviation from the averaged value. Therefore, an uncertainty of  $\pm 3$  ns can be assumed in the data points.

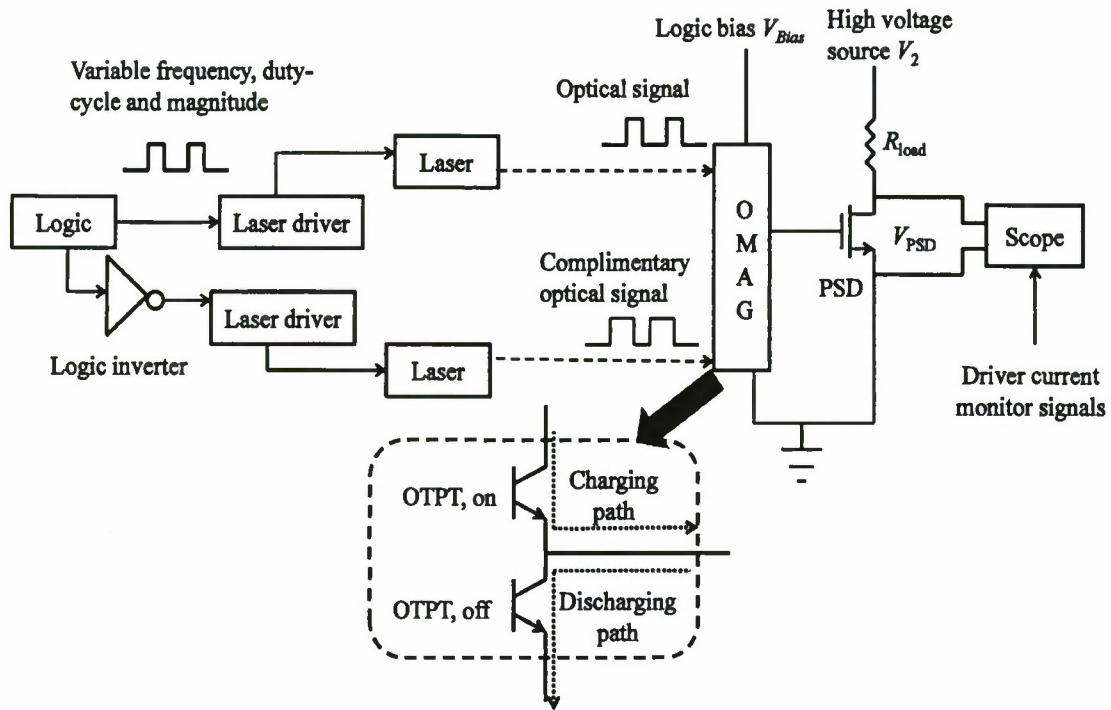
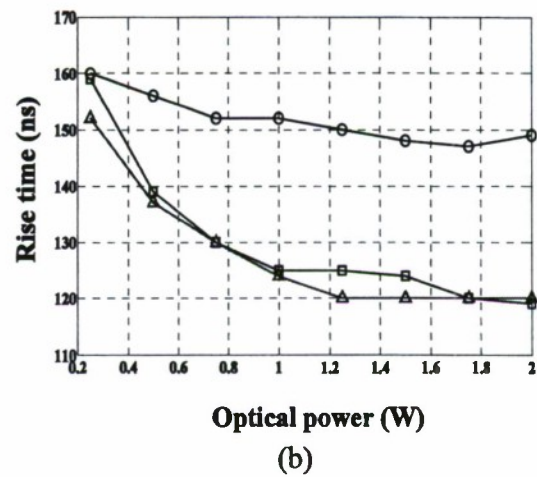
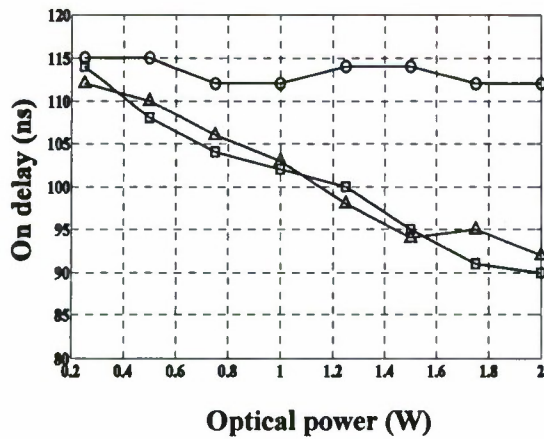
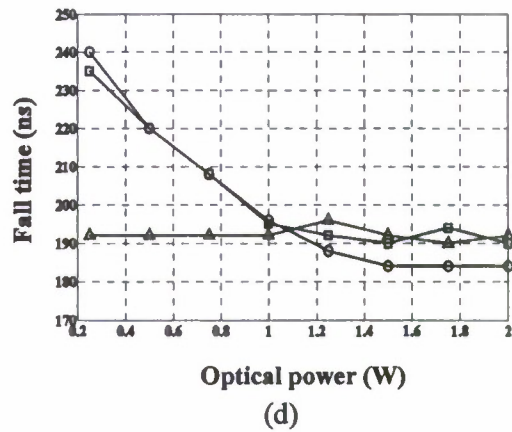
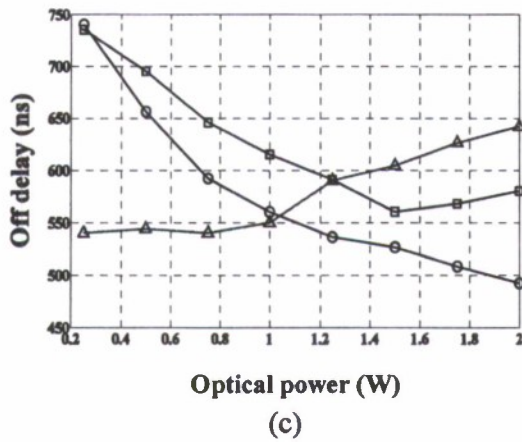


Fig. 37: (a) O MAG (full-controllability architecture) coupled to PSD – schematic of the experimental circuit.





On laser variation  
 Off laser variation  
 On and off laser variation

Fig. 38: Modulation of (a) turn-on delay, (b) rise time, (c) turn-off delay, and (d) fall time of 47N50 CoolMOS™ with varying optical power. Logic bias  $V_1 = 12$  V,  $V_2 = 50$  V,  $R_{load} = 40 \Omega$ , frequency – 30 kHz, duty cycle – 50%.

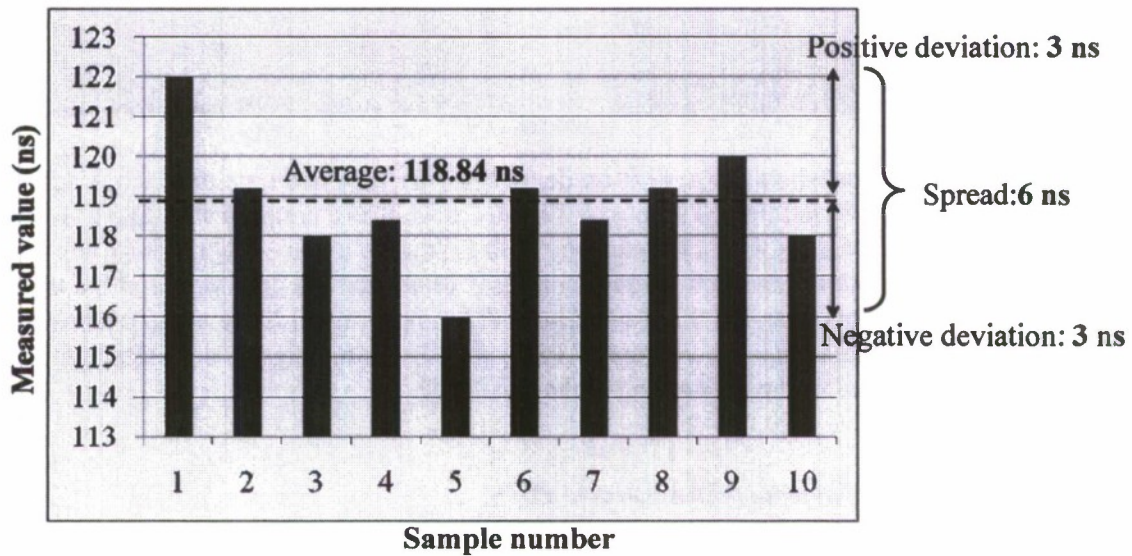
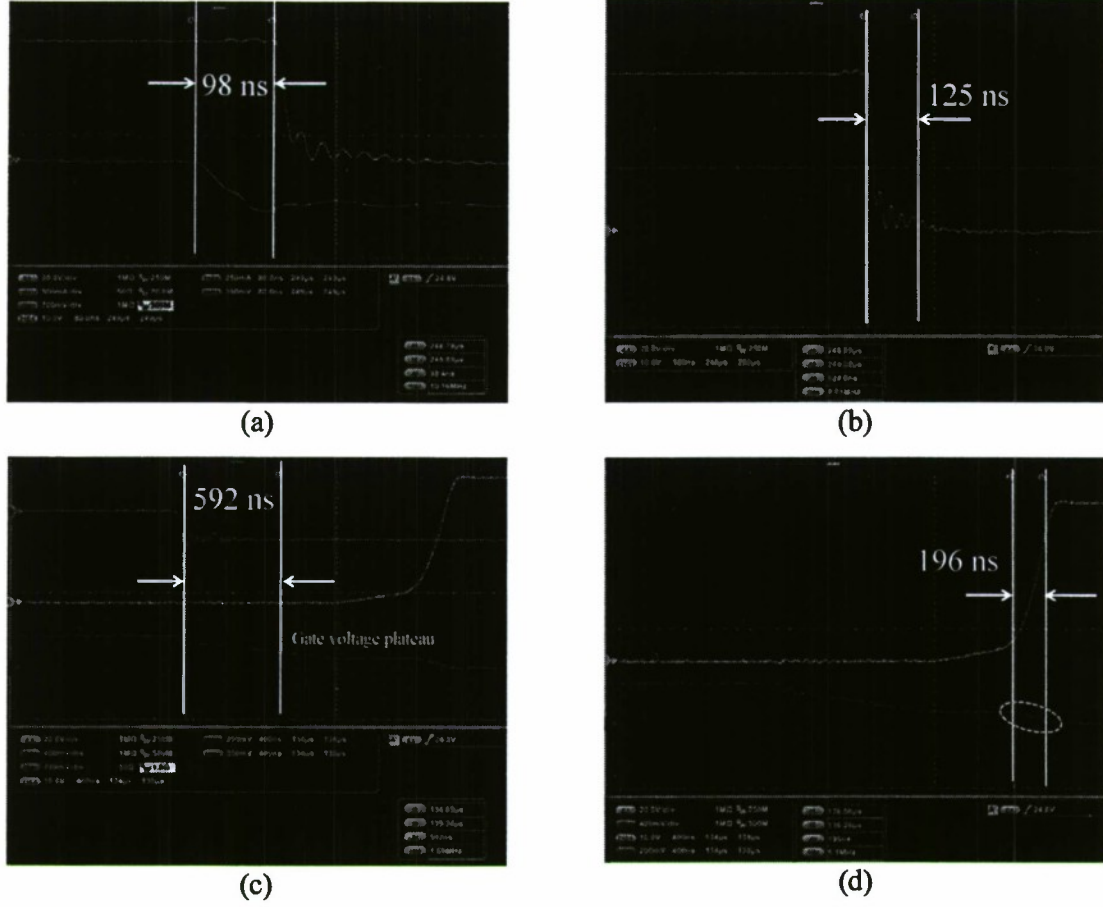


Fig. 39: Statistical distribution of the randomly measured rise time data for PSD coupled with OMAG. Maximum deviation is  $\pm 3$  ns.





**Fig. 40:** Time-domain snapshots of (a) turn-on delay (98.4 ns), (b) rise time (124.8 ns), (c) turn-off delay (592 ns), and (d) fall time (196 ns) of 47N50 CoolMOS™ coupled with OMAG. Logic bias  $V_1 = 12$  V,  $V_2 = 50$  V,  $R_{load} = 40$   $\Omega$ , frequency = 30 kHz, duty cycle = 50%. For (a) top signal is the voltage across PSD and bottom signal is on-laser drive; for (b) only signal is the voltage across PSD; for (c) the topmost signal is the off-laser drive, next signal is the voltage across PSD and bottom signal is the gate-source voltage of PSD; for (d) the top signal is the voltage across PSD and the bottom signal is the gate-source voltage of PSD.

### 5.5. Scalability of optical control with respect to PSD

The advantage of employing a hybrid structure (comprising of front-end optical-triggering structure coupled with PSD) can be leveraged as the dimension of optical-triggering structure does not need to be scaled up in the same proportion as that of the main power semiconductor device. This can potentially keep the optical-triggering power requirement low even for a higher voltage and current rated PSD. The primary function of the optical-triggering signal becomes modulating the conductivity of the front-end optical device so that they control the charging and discharging dynamics of the PSD gate terminal accordingly thereby controlling the overall switching behavior.

It can be concluded that the de-coupling of optical-triggering power requirement and electrical conduction through the PSD facilitates the scalability of PSD in terms of voltage, current, structural details and material. The fundamental idea is to use uniform optical-triggering structure across many variations of the PSD. A case illustration is shown schematically in Fig. 41.

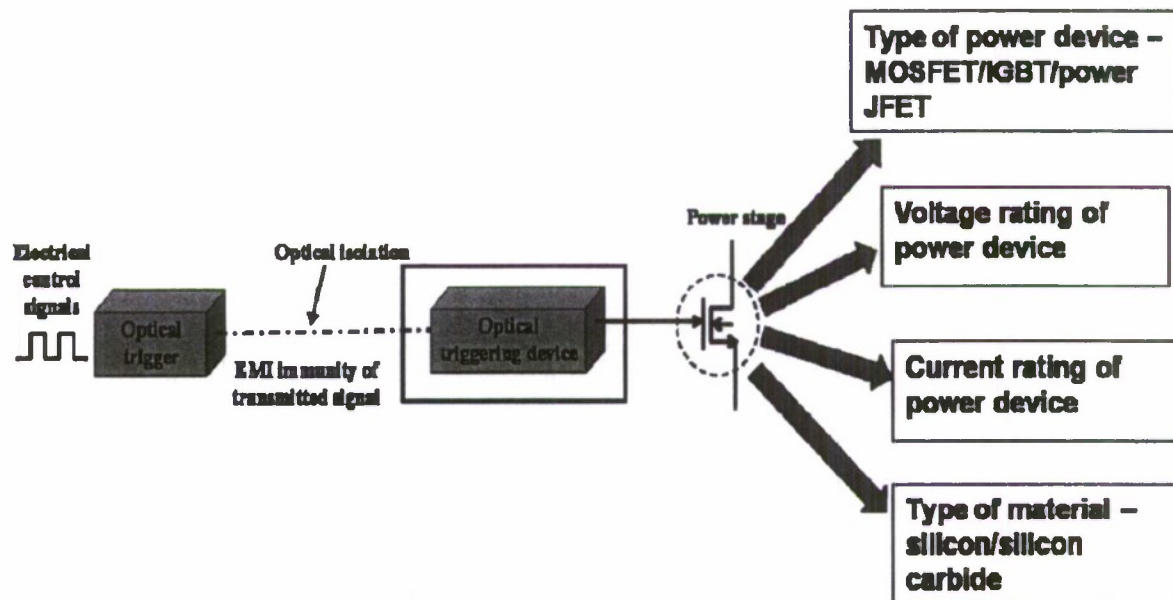
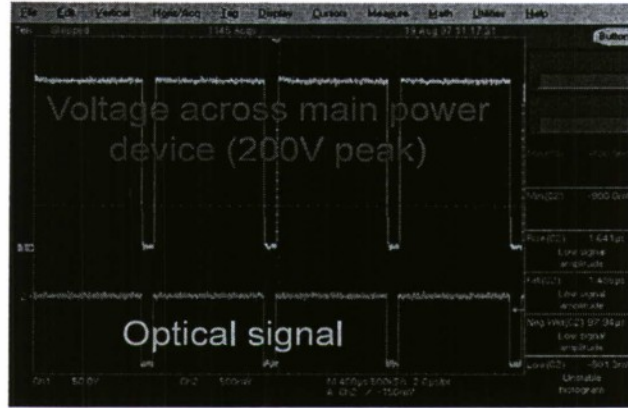


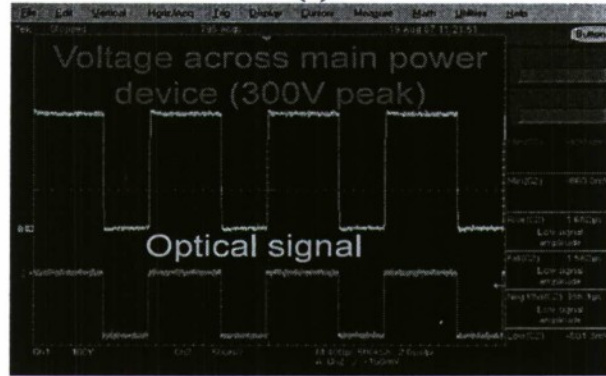
Fig. 41: Illustration of the scalability issues with respect to the PSD.

As the voltage or current rating of the PSD varies, the input impedance of the device varies. With variation across device structure or material, this change is even more significant. Consequently, the nature and extent of interaction between the optical-triggering device and the PSD needs to be studied in depth to analyze the effect of scalability on the switching dynamics of the overall hybrid device structure.

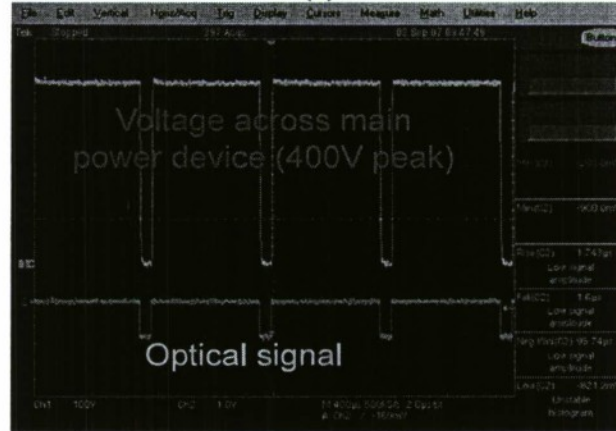
Voltage scalability of the optical-triggering concept was demonstrated by showing the nominal switching operation with identical optical power but using PSDs of different voltage rating. Silicon MOSFETs of 300 V, 400 V, and 600 V breakdown ratings were used for the experiment. The same OTPT was coupled, in turn, to these devices following identical circuit arrangement (as in Fig. 37). The actual load voltages applied were 200 V, 300 V and 400 V, respectively. Load resistors were adjusted in each case to keep the load current at the same level. Representative switching results are shown in Fig. 42. For all the PSD of different voltage ratings, the drain-source voltage follows the optical control signal closely over a wide range of frequency and pulse-width.



(a)



(b)



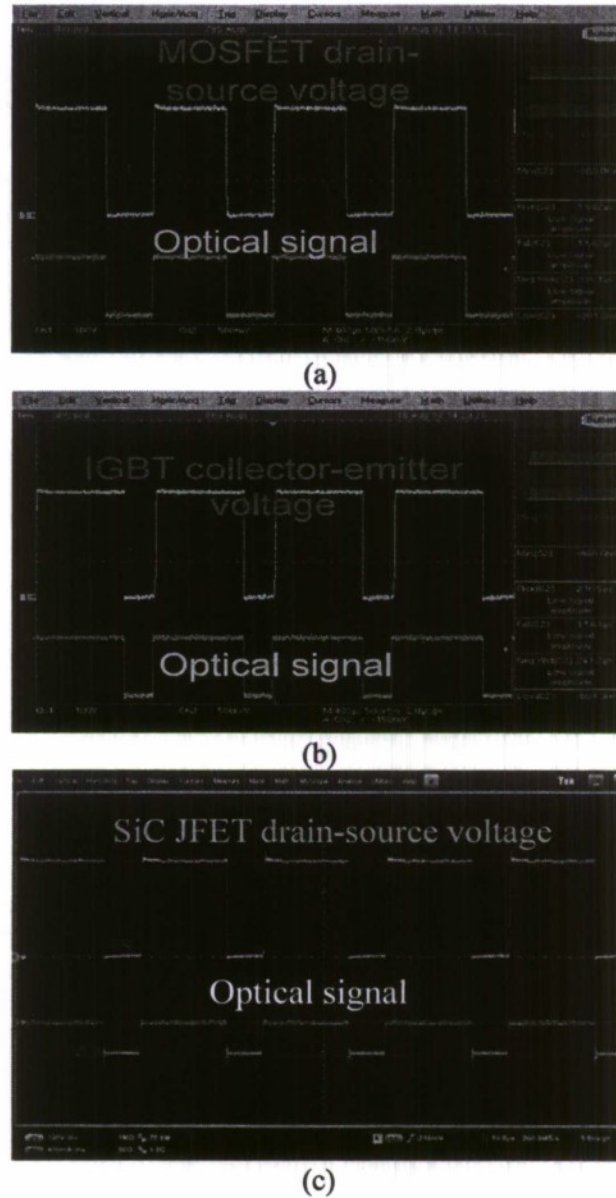
(c)

**Fig. 42:** Demonstration of voltage scalability – switching with identical optical power, power devices of (a) 200V, (b) 300V, (c) 400V. Scale - vertical axis: 100 V/div, horizontal axis: 400  $\mu$ s/div. Logic bias  $V_1 = 12$  V,  $V_2 = 300$  V,  $R_{gate} = 10 \Omega$ ,  $R_{load} = 1000 \Omega$ , frequency = 1 kHz, duty cycle = (a) 10%, (b) 25%, (c) 10%.

Next, we demonstrate the scalability of the optical-triggering in terms of PSD structure and material. The same OTPT was coupled, in turn, to silicon MOSFET, silicon IGBT and 4H-SiC based vertical JFET (obtained from SiCED AG, Germany) following identical circuit



arrangement (as in Fig. 37). Nominal switching operation with identical optical power but these different PSD was tested. Representative switching results are shown in Fig. 43. For all the PSD types, the drain-source voltage of the PSD follows the optical control signal closely over a wide range of frequency and pulse-width.



**Fig. 43:** Demonstration of material and structural scalability – switching with identical optical power, power devices of (a) silicon MOSFET, (b) silicon IGBT, and (c) SiC based vertical JFET. Scale - vertical axis: 100 V/div, horizontal axis: (a) and (b) 400  $\mu\text{s}/\text{div}$ , (c) 10  $\mu\text{s}/\text{div}$ . Logic bias  $V_1 = 12\text{ V}$ ,  $V_2 = 300\text{ V}$ ,  $R_{\text{gate}} = 0$ ,  $R_{\text{load}} = 1000\ \Omega$ .

### 5.6. Integrated packaging of GaAs OTPT with different types of PSDs

After demonstrating the nominal operation and optical intensity modulation effects with discretely coupled OTPT and PSD, integrated packaging of OTPT and PSD is considered. Instead of using packaged PSD, commercially available dies of Si power MOSFET, IGBT, and SiC VJFET are obtained and co-packaged with OTPT die. The aim of such hybrid packaging is to reduce the interconnect length thereby minimizing interconnect parasitic impedance between the OTPT and the PSD. This is an important factor which may be significant for high-power, high-frequency operation where interconnect parasitic impedance can introduce high peak-value over-voltage or over-current transient during rapid switching. Minimizing such parasitic potentially enhances the reliability of the overall device and leads to a robust power electronic system. Furthermore, the optical fiber can be terminated into a single hybrid package thereby enhancing the immunity of the PSD as well as the OTPT-PSD interconnects to external electromagnetic interference.

Key issues for such integrated packaging are the mutual placement of OTPT and the PSD dies. Most often the PSD die (for all the cases of our choice) is a vertical device with bond pads on both sides of the die whereas the bond pads of OTPT are on the top side of the die and the backside is not metalized. Therefore, the bottom bond pad of the PSD die needs to be soldered onto a conductive metal pad from which bond wire can be brought out for external connection. Furthermore, both OTPT and the PSD die needs to dissipate heat through the package floor while in operation. However, the dies cannot be directly attached to the package floor as their backside cannot be at the same electrical potential. Dies, therefore, must be pasted to a thermally conductive but electrically insulating die-attach material (beryllium oxide was chosen for this case) which helps conduction of heat but provide necessary electrical isolation. The scheme is illustrated in Fig. 44. Actual packaged device prototypes are shown in Fig. 45.

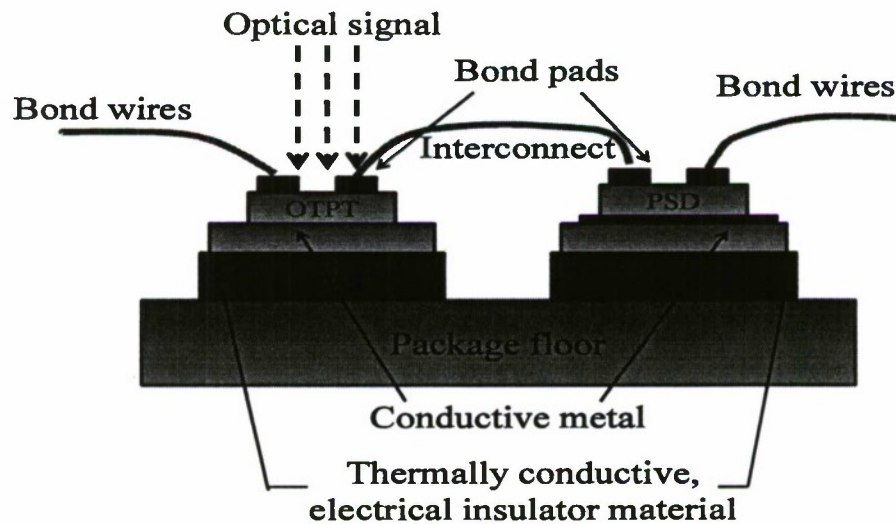
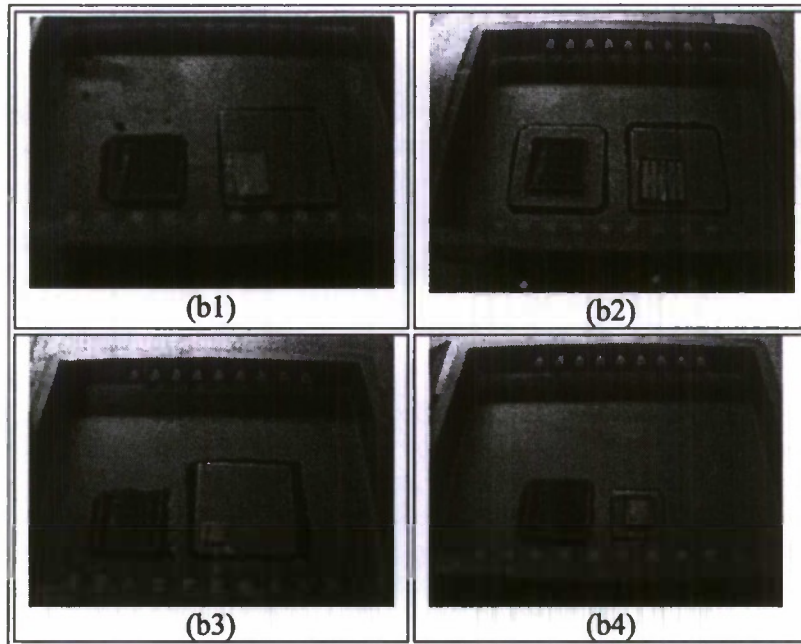


Fig. 44: Integrated packaging scheme showing the bond wires, interconnects, die attach material.



**Fig. 45:** Prototype packaged devices – OTPT coupled with (b1) 600 V Si power MOSFET (from International Rectifier), (b2) 600 V silicon IGBT (from International Rectifier), (b3) 600 V SiC VJFET (from SiCED AG), and (b4) 1200 V SiC power MOSFET (from Cree Inc.).

## 6. OPTICAL INTENSITY MODULATED SYSTEM PERFORMANCE PARAMETERS

The concept of optical intensity modulation is extended to investigate how it affects the system level performance parameters. While increasing optical power improves efficiency, it may degrade the parasitic noise performance and stress level (by producing faster rate of change in voltage and current). Therefore the necessity of an optimization is discussed and the technical approach to obtain such optimized value is illustrated. Because, apart from the optical-triggering power, large number of system operating conditions and particular type of PSD also affect the performance parameters, it is argued that an experimentally measured mapping technique to correlate optical power to system performance parameters (at a given operating condition) would be useful.

For experimental characterization, a dc-dc step-down switching converter is built using OTPT as the triggering structure for the PSD and experiments are conducted on this circuit. Power conversion efficiency was measured by varying optical-triggering power at a fixed load power as well as over a range of load power. Optical intensity modulated rate of change of voltage across the PSD is also measured.



### 6.1. Optical intensity modulation of power conversion efficiency

In a switching power converter, the rise and fall times of a PSD govern the switching loss ( $L_{sw}$ ) and also the turn-on and turn-off delay can add to the loss. The power conversion efficiency of a power converter, typically, can be expressed as,

$$\eta = \frac{P_{load}}{P_{load} + N(L_{cond} + L_{SW}) + L_{para}} \quad (40)$$

where  $P_{load}$  is the output load power,  $N$  is the number of simultaneously active PSDs in the converter circuit,  $L_{cond}$  is the conduction loss of the PSD, and  $L_{para}$  is the parasitic losses (for example loss due to energy storage elements in the circuit i.e. inductor core and copper loss, capacitor resistive loss etc.). Now, by optical power modulation we control primarily switching loss i.e.  $L_{SW}$ . Therefore, we express this loss in terms of OTPT parameters. However, different analytical expressions would evolve when different types (e.g. MOSFET, IGBT, JFET etc) of PSD would be coupled to OTPT. For a specific illustration, we take a case of a power MOSFET as a PSD. Analytical expression for switching loss for such a PSD is given by [27],

$$L_{SW} = f_{SW} \cdot \frac{V_{in} I_{in}}{2} [t_r + t_f] \quad (41)$$

where  $f_{SW}$  is the switching frequency,  $V_{in}$ ,  $I_{in}$  are the average voltage across and current through the power MOSFET and  $t_r$  and  $t_f$  are the rise and fall times respectively of the PSD i.e. power MOSFET. As seen from the previous discussions, the rise time and delays are dependent on the optical power and therefore the switching loss should also be a function of optical power.

To demonstrate the modulation of power conversion efficiency, a non-synchronous buck converter was built where the PSD is a 100V, 10A rated MOSFET (part number IRF530) triggered by the OTPT. The circuit schematic is illustrated in Fig. 46 and the actual circuit is shown in Fig. 47.

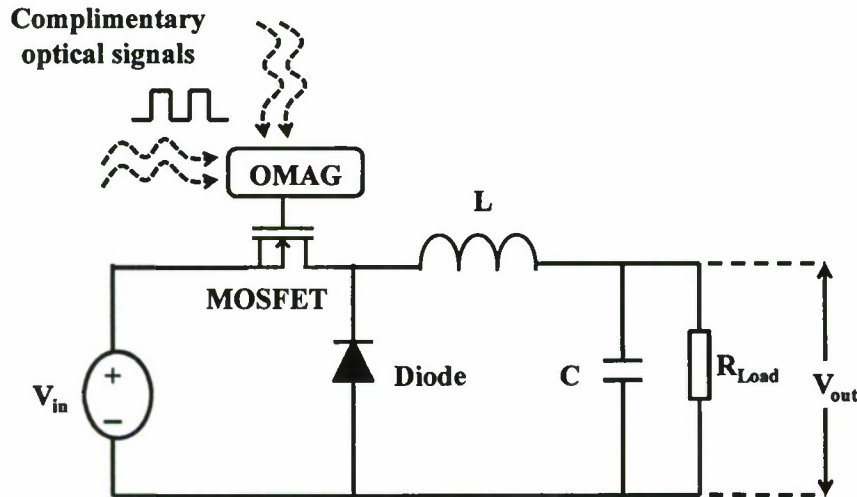


Fig. 46: Circuit schematic of the buck converter controlled by OMAG with full controllability (using two complimentary optical signals).

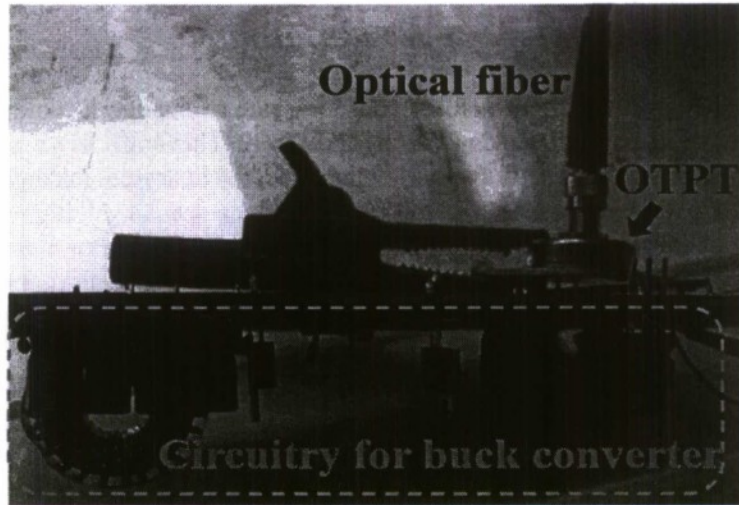
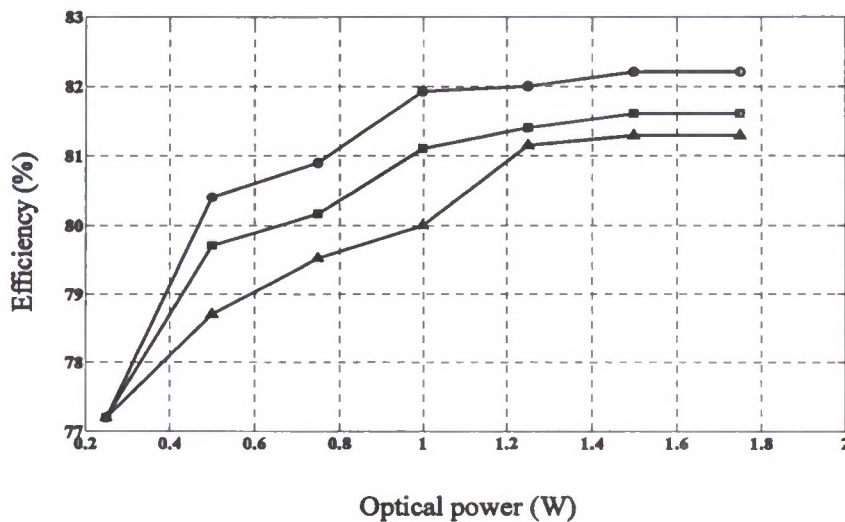


Fig. 47: Side view of the buck converter with optical-triggering structure.

We measure the power conversion efficiency by measuring the ratio of output and input power. The efficiency ( $\eta$ ) is given by,

$$\eta = \frac{P_{out}}{P_{in}} = \frac{V_{out}^2 / R_{Load}}{V_{in} \cdot I_{in}} \quad (42)$$

where  $R_{Load}$  is the load resistance and  $I_{in}$  is the average DC input current. We vary the optical-triggering power and measure corresponding power conversion efficiency values. The modulation of power conversion efficiency with optical power is plotted in Fig. 48.



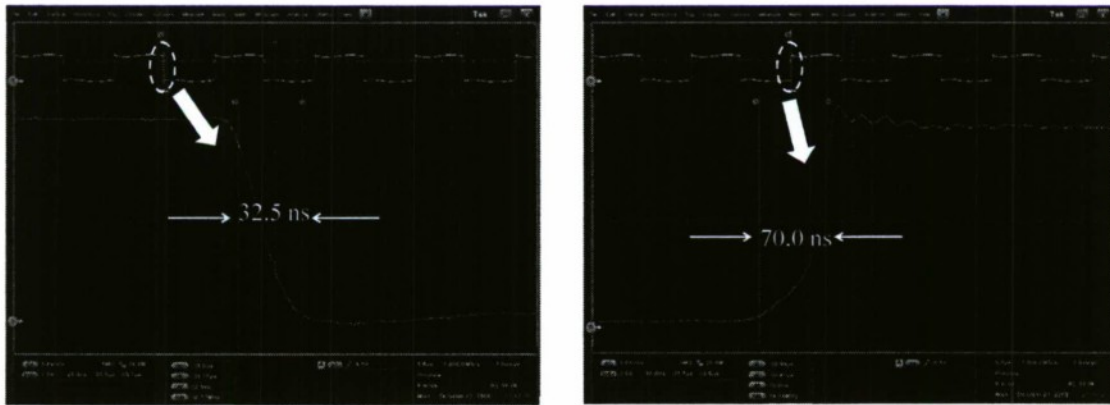
—○—○—○—○— Full control    —□—□—□—□— Turn-on control    —△—△—△—△— Turn-off control

Fig. 48: Buck converter efficiency modulated by optical power variation at a fixed load power for three different OMAG architectures.  $V_{in} = 20$  V, frequency = 100 kHz, duty cycle = 50%,  $R_{load} = 5 \Omega$ , load power = 20 Watt.

## 6.2. Optical intensity modulation of $dv/dt$ and $di/dt$ stress

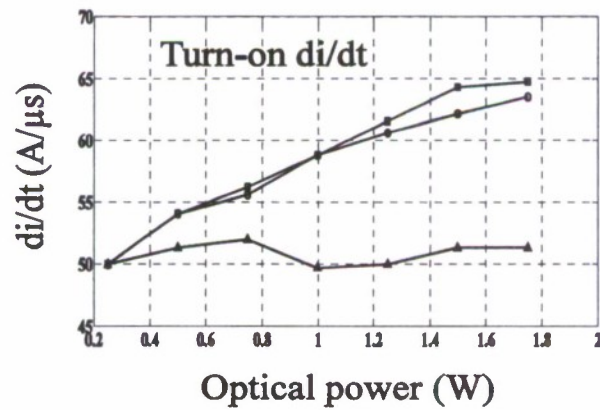
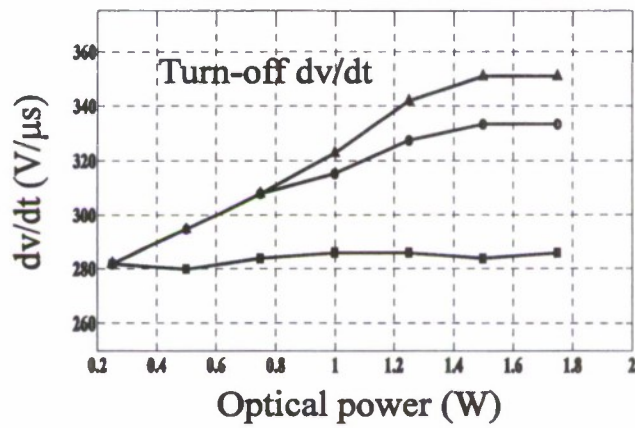
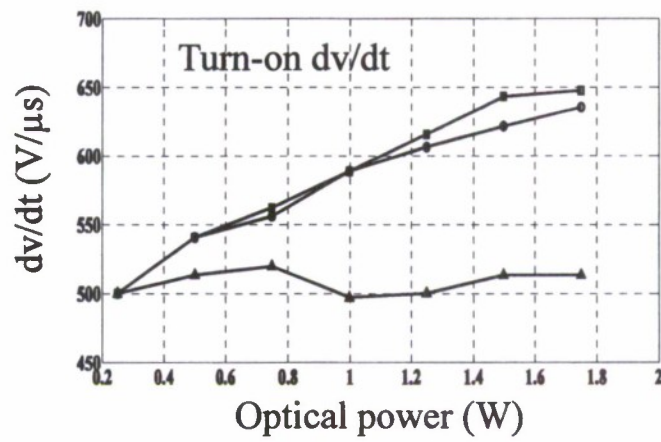
Transient induced electrical stress results from high rate of change in voltage ( $dv/dt$ ) across a device or high rate of change of current ( $di/dt$ ) through it. This high  $dv/dt$  or  $di/dt$ , along with device parasitic capacitance or circuit parasitic elements (for example, leakage inductance of the transformer in an isolated converter topology), can induce transitory high voltage or current signals which can affect the devices, disrupt nominal circuit operation or can even aggravate the reliability of the system operation. Because the optical intensity modulation causes variation in rise and fall time of a PSD, it is also expected to influence the  $dv/dt$  and  $di/dt$  rate of a PSD in a converter.

Assuming a linear rate of change in the voltage across PSD turning on, the  $dv/dt$  rate can be calculated approximately by dividing the peak voltage by the rise time. Because the rise time of the PSD is dependent on the optical power level, the  $dv/dt$  is also expected to vary with optical power. Similarly, the rate of change of current i.e.  $di/dt$  can be calculated from the rise time and peak current flowing through the PSD. From the same buck converter setup we measure the  $dv/dt$  and  $di/dt$  rate of the PSD by physically examining the rise and fall times and using those values along with peak voltage and current stress on the PSD. Now, voltage and current changes sharply both during turn-on and turn-off instant, we measure the variation of the  $dv/dt$  and  $di/dt$  with optical power for turn-on and turn-off and also for all three architectures i.e. (a) only turn-on dynamics controlled actively by optical intensity, (b) only turn-off dynamics controlled actively by optical intensity, and (c) both turn-on and turn-off dynamics controlled actively by optical intensity. Representative time-domain results (rise and fall time of voltage across PSD) are shown in Fig. 49 and parametric variations of  $dv/dt$  and  $di/dt$  rate are plotted in Fig. 50.



**Fig. 49:** A representative time-domain result showing the rise and fall time of the voltage across the PSD in the buck converter during nominal operation.





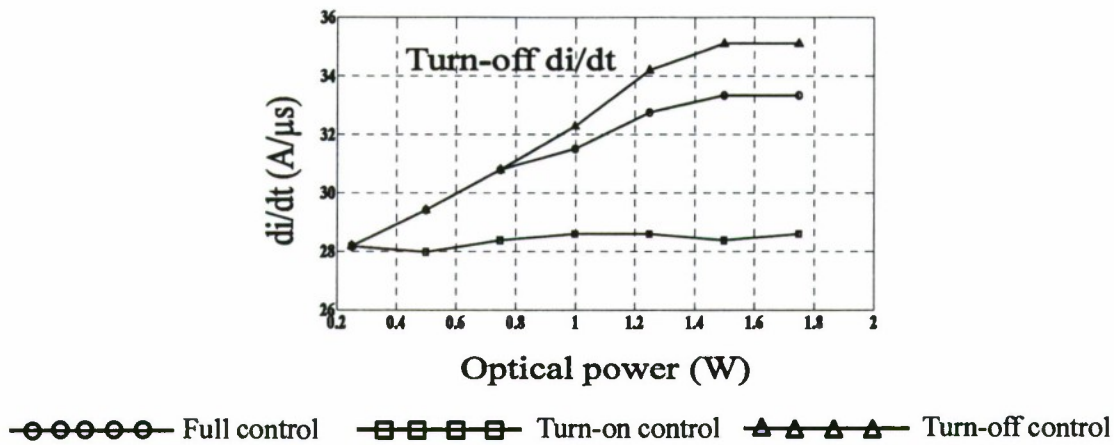


Fig. 50 Modulation of  $dv/dt$  and  $di/dt$  rate of the PSD with varying optical power in the buck converter prototype (shown both for turn-on and turn-off instant).

### 6.3. Optical intensity modulation of electromagnetic noise

Conducted and radiated noise from power electronics system are ubiquitous and demand significant attention in the design and layout phase [28]. Noise generated by power converters can affect the operation of nearby low-power microelectronic circuits and equipments controlled by them [29, 30]. There exist strict limits (national and international standard specifications) on the magnitude of these noise spectrums for various commercial, residential and military application domains (Web source: <http://www.smeps.com/Knowledge/Standards/EN50082-1.htm>). Numerous techniques have been proposed and put into practice for reducing or attenuating these noises over a range of frequency – EM shielding, layout with reduced parasitic [31], EMI filter [32], soft switching [33], chaotic modulation [34], random/programmed frequency modulation [35] etc. EM shielding attenuates predominantly the radiated noise level at a given distance from the converter while it does not directly address the reduction of noise generation. Filtering techniques attenuates the noise amplitude over a range of frequency while frequency modulation techniques shapes the frequency spectrum of the noise in such manner (by redistributing a portion of noise energy among multiple sideband frequencies) that the peak amplitude remains lower than the prescribed standard. Reducing parasitic elements by novel layout addresses the fundamental cause of the noise generation but it is limited in scalability and reproducibility in the sense that unique layout optimization is often needed for a given circuit and therefore no generalized procedure can be formulated. However, there have been limited works focusing on the control of the noise by controlling the fundamental source – dynamics of the switching phenomenon.

Rapid switching events of PSDs in a power electronics system produce fast changes in voltage and current (i.e.  $dv/dt$  and  $di/dt$ ) and contribute significantly to the conducted and radiated parasitic noise generated by the switching system [36, 37]. Studies have shown that in pulse-width modulated (PWM) AC drives, pulse rise time has a significant effect on the noise energy coupling to the circuit [38]. The entire frequency spectrum changes with the rise and fall time of the switches [39]. Apart from conducted noise, generated by circuit parasitic elements, analyses on the radiated noise illustrate the role of device switching parameters (e.g. rise time)

on the amplitude and envelope of the noise [40]. Gate drive circuit with separate on and off-state gate resistances has been proposed and the improvement in parasitic noise has been shown with slowing down pulse edges [41]. If the switching dynamics (rising and falling edges) of PSD can be controlled optically and dynamically without physically altering any circuit components, optical modulation is expected to affect the system-generated parasitic noise.

We investigate this hypothesis experimentally by varying the optical power and measuring the frequency spectrum of the input current waveform of the buck converter. The measurement schematic is shown in Fig. 51. Agilent spectrum analyzer 4395A is used to capture the frequency domain representation of the input current waveform. High-bandwidth, Hall-sensor current probe is placed around the input cable and it is connected to the spectrum analyzer through 50Ω BNC termination. Analyzer output is connected to a PC and the spectrum data (frequency vs. amplitude) is directly captured through GPIB-USB interface. Input voltage, optical duty-cycle, switching frequency and load resistance values are kept unchanged. Generally, for conducted noise measurement, the industry standard frequency band is 10 kHz-5 MHz (for radiated noise it is 5 MHz – 30 MHz). Accordingly, the low and high frequency limits were set at 10 kHz and 5 MHz with a 1 kHz resolution in the analyzer. Optical power was varied in three discrete steps from 500 mW to 1.5 W to 2.5 W. Both input positive and negative lead (return path) current spectrum data was measured for each case. From measurement point of view (Fig. 51), common mode noise can be obtained by [42],

$$I_{CM} = I_{+,in} + I_{-,in} \quad (43)$$

where  $I_{+,in}$  and  $I_{-,in}$  are the positive and negative lead current respectively. Consequently, we add these two current spectrum data and plot the results. Corresponding results are shown in Fig. 52. The envelope of the spectrum is drawn for the third case (2.5 W) by joining the peaks of the magnitudes.

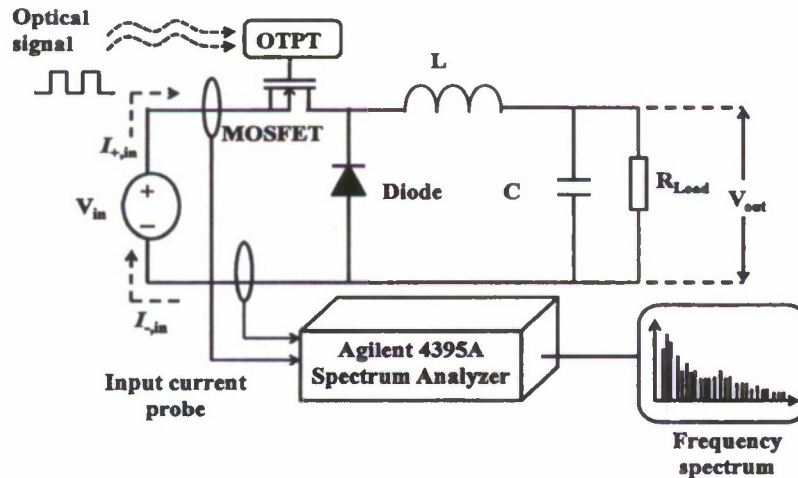
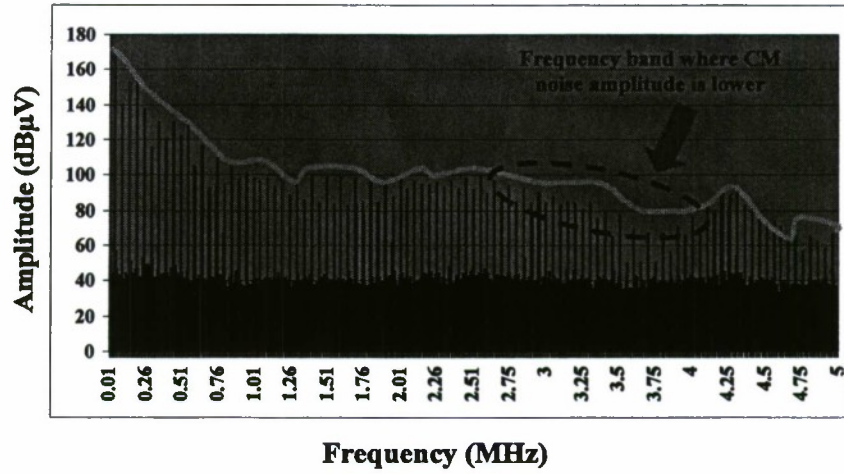


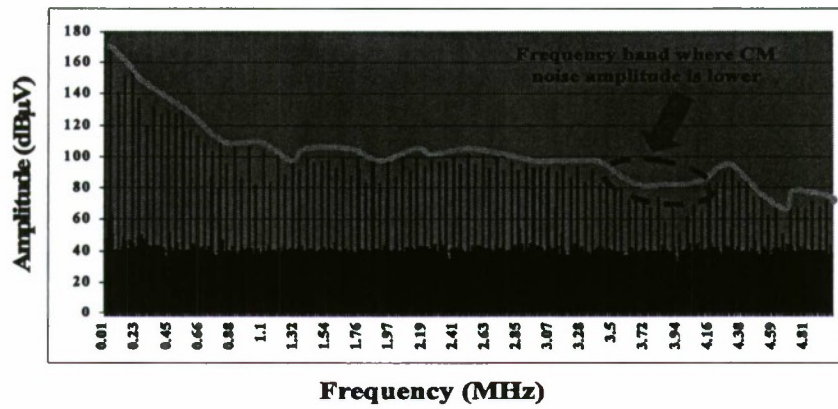
Fig. 51: Experimental schematic for measurement of conducted parasitic noise spectrum of the converter and how it varies with optical power.

Exactly same envelope, when superimposed on the other two, illustrates the changes in the spectrum, occurred purely due to optical power variation. Smaller optical power lowers the common mode noise amplitudes in certain frequency ranges because of slower switching transition speed.

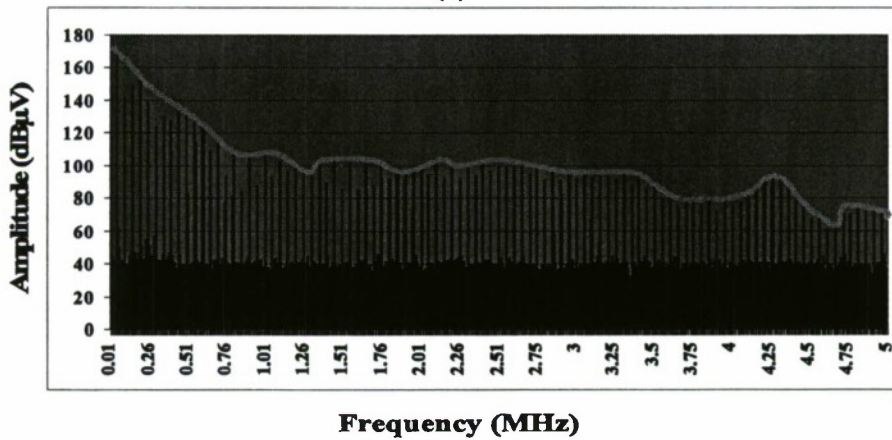




(a)



(b)



(c)

**Fig. 52:** Conducted noise frequency spectrum (measured over 10 kHz-5 MHz @ 1 kHz resolution) for three optical power levels at (a) 500 mW, (b) 1.5 W and (c) 2.5 W with exactly same envelope.

## 7. SUMMARY OF THE PROJECT TASKS AND RESEARCH FINDINGS

### 7.1. *Summary of the work*

We summarize the key tasks performed in this project as follows,

- Physics based and simulation studies of GaAs based optically-triggered power transistor (OTPT) are performed. Detailed process simulations and process-flow design optimization are done.
- Fabrication of the prototype device is carried out and packaging and optical interfacing is designed and implemented subsequently. An optical test-bench (including light source, driver, optical fiber etc) for switching characterizations is designed.
- Characterization results of the single OTPT device are detailed including optical pulse-following over wide range of duty cycle and frequency.
- Physics based modeling and simulation studies on the OTPT conductivity and switching parameters variation with optical power are discussed and subsequent characterization results are demonstrated.
- OTPT is coupled to power semiconductor device (PSD) and optical intensity modulation of the switching dynamics of the PSD is analyzed and experimentally characterized by varying optical power level and measuring switching parameters.
- Scalability of optical-triggering in terms of PSD voltage, material platform, and structural variations are illustrated experimentally. After showing the experimental characterizations with discrete coupling of OTPT and PSD, an integrated hybrid packaging scheme is also discussed and the package assembly design is illustrated along with fabricated prototypes.
- Modulation of power electronics system performance parameters with optical intensity levels is illustrated experimentally by building a dc-dc, non-synchronous buck converter with OTPT driving a power MOSFET. Power conversion efficiency,  $dv/dt$  and  $di/dt$  stress of the PSD in the converter, and conducted electromagnetic noise are measured for varying optical power levels and the corresponding modulations are demonstrated.

### 7.2. *Key research findings*

We summarize the key findings of this work as follows,

- Optical intensity modulation causes nonlinear variation in the conductivity (or resistivity) of OTPT. When OTPT is coupled to the PSD, this variation translates into variable rate of charging/discharging of the input capacitance of the PSD and thereby can control the switching dynamics of the PSD.
- Optical control and intensity modulation of switching dynamics works over a wide range of PSD types, material platforms, different structures and voltage and current ratings although the exact range and sensitivity of the modulation may vary.
- Because the switching dynamics of the PSD is intrinsically linked to system level parameters such as power conversion efficiency,  $dv/dt$  and  $di/dt$  stress and electromagnetic noise emission from a power converter, concept of optical intensity modulation can also be extended to the domain of system parameter control.

- It has been observed from the experimental results and theoretical analyses that whereas converter efficiency increases (i.e. converter loss decreases) with increasing optical power, this is also accompanied by an increase in  $dv/dt$  and  $di/dt$  stress. Therefore, although increasing optical power minimizes loss, it maximizes the  $dv/dt$  which is not desirable. This observation leads to the possibility of building an optimization framework which will help deciding an optimal level of optical intensity for a given operating condition in a power converter.



## REFERENCES

1. J.J. Ely, G.L. Fuller, and T.W. Shaver, "Ultrawideband electromagnetic interference to aircraft radios", *Digital Avionics Systems Conference*, Vol.2, pp. 13E4-1 - 13E4-12, 2002.
2. J.R. Todd, "Direct optical control: a lightweight backup consideration", *IEEE National Aerospace and Electronics Conference*, Vol: 2, pp. 456 – 463, 1992.
3. <http://www.afrlhorizons.com/Briefs/Apr05/VA0412.html>.
4. S.K. Mazumder and T. Sarkar, "Optically-triggered power transistor (OTPT) for fly-by-light (FBL) and EMI-susceptible power electronics", Plenary Paper, *IEEE Power Electronics Specialists Conference*, pp. 1-8, 2006.
5. T. Sarkar and S. K. Mazumder, "Epitaxial Design and Sensitivity Studies for Optically-triggered GaAs-AlGaAs Superjunction Heterostructure Power Device", *IEEE Transactions on Electron Devices*, Vol. 54, Issue: 4, pp. 589-600, 2007.
6. S.K. Mazumder, T. Sarkar, M. Dutta, and M. S. Mazzola, "Photoconductive Devices in Power Electronics", *Electrical Engineering Handbook*, 3<sup>rd</sup> Ed., Taylor & Francis, pp. 9-42, 2006.
7. T. Sarkar and S. K. Mazumder, "Dynamic power density, wavelength, and switching time modulation of optically-triggered power transistor (OTPT) performance parameters", *Microelectronics Journal*, Vol. 38, pp. 285-298, 2007.
8. A. Rosen and F. Zutavern, *High Power Optically Activated Solid-State Switches*, Artech House, MA, 1994.
9. C. Furbock, R. Thalhammer, M. Litzenberger, N. Seliger, D. Pogany, E. Gornik, and G. Wachutka, "A differential backside laserprobing technique for the investigation of the lateral temperature distribution in power devices", *International Symposium on Power Semiconductor Devices and ICs*, pp. 193 – 196, 1999.
10. P. Jacob, "Defect- and structure-weakness-localization on power semiconductors using OBIRCH (optical beam induced resistivity change)", *International Symposium on the Physical and Failure Analysis of Integrated Circuits*, pp. 152 – 156, 2002.
11. T. Yamagata, T. Sakai, K. Sakata, K. Shimomura, "High current modulation in optically controlled MOSFET using directly-bonded SiO<sub>2</sub>-InP", *International Topical Meeting on Microwave Photonics*, pp. 173 – 176, 1996.
12. T. Yamagata and K. Shimomura, "High responsivity in integrated optically controlled metal-oxide semiconductor field-effect transistor using directly bonded SiO<sub>2</sub>-InP", *IEEE Photonics Technology Letters*, Vol: 9, pp. 1143 -1145, 1997.
13. AAA De Salles, "Optical control of GaAs MESFET's", *IEEE Transactions on Microwave Theory and Techniques*, Vol: 31, No. 10, pp. 812-820, 1983.
14. Shubha, B.B. Pal, and R.U. Khan, "Optically-controlled ion-implanted GaAs MESFET characteristic with opaque gate", *IEEE Transactions on Electron Devices*, Vol: 45, Issue: 1, pp. 78 – 84, 1998.

15. P. Chakrabarti, S.K. Shrestha, A. Srivastava, and D. Saxena, "Switching characteristics of an optically controlled GaAs-MESFET", *IEEE Transactions on Microwave Theory and Techniques*, Vol: 42, Issue: 3, pp. 365 – 375, 1994.
16. D.M. Kim, S.H. Song, H.J. Kim, K.N. Kang, "Electrical characteristics of an optically controlled N-channel AlGaAs/GaAs/InGaAs pseudomorphic HEMT", *IEEE Electron Device Letters*, Vol: 20, Issue: 2, pp. 73-76, 1999.
17. G. Vitale, G. Busatto, and G. Ferla, "The switching behavior of the bipolar mode field effect transistor (BMFET)", *IEEE Industry Applications Society Annual Meeting.*, Vol: 1, pp. 600 – 605, 1988.
18. G. Breglio, R. Casavola, A. Cutolo, and P. Spirito, "The bipolar mode field effect transistor (BMFET) as an optically controlled switch: numerical and experimental results", *IEEE Transactions on Power Electronics*, Vol: 11, Issue: 6, pp. 755 – 767, 1996.
19. T. Sarkar and S.K. Mazumder, "Amplitude, Pulse-Width, and Wavelength Modulation of a Novel Optically-Triggered Power DMOSFET", *IEEE Power Electronics Specialists Conference*, pp. 3004-3008, 2004.
20. M.J. Lazarus, K. Loungis, and V.H.W. Allen, "Optically controlled high-speed switching of a power transistor", *IEEE Transactions on Circuits and Systems I: Fundamental Theory and Applications*, Vol: 47, Issue: 4, pp. 528–535, 2000.
21. P. Bhadri, D. Sukumaran, K. Ye, S. Dasgupta, E. Gulians, F.R. Beyette, Jr., "Design of a smart optically controlled high power switch for fly-by-light applications", *IEEE Midwest Symposium on Circuits and Systems*, Vol. 1, pp. 401–404, 2001.
22. S.M. Sze, *Semiconductor Devices: Physics and Technology*, Wiley & Sons, 2001.
23. M. Brozel, and G. Stillman, *Properties of gallium arsenide*, INSPEC, Institution of Electrical Engineers, 1986.
24. S. Adachi, "GaAs, AlAs, and  $\text{Al}_x\text{Ga}_{1-x}\text{As}$ : Material parameters for use in research and device applications", *Journal of Applied Physics*, vol. 51, Issue: 3, 1985.
25. S.K. Mazumder and T. Sarkar, "Optical Modulation for High Power Systems: Potential for Electromagnetic-Emission, Loss, and Stress Control by Switching Dynamics Variation of Power Semiconductor Devices", *Proceedings of IEEE Energy 2030 Conference*, 2008.
26. V. Benda, J. Gowar, D.A. Grant, *Power Semiconductor Devices*, Wiley & Sons, West Sussex, England, 1999.
27. N. Mohan, T.M. Undeland, and W.P. Robbins, *Power Electronics: Converters, Applications, and Design*, 3<sup>rd</sup> edition, Wiley & Sons, 2002.
28. R. Redl, "Power Electronics and Electromagnetic Compatibility", *IEEE Power Electronics Specialist Conference*, vol. 1, pp. 15-21, 1996.
29. R. Redl, P. Tenti, and J.D. van Wyk, , "Power electronics' polluting effects", *IEEE Spectrum*, vol. 34, Issue: 5, pp. 32-39, 1997.
30. Fiori, F., "EMI-induced failures in PWM controllers for SMPS", *EMC Europe*, pp. 410-413, 2004.



31. E. Persson, "Power electronic design and layout techniques for improved performance and reduced EMI", *Proceedings of Power Electronics in Transportation*, pp. 79-82, 1994.
32. S. Ogasawara, H. Ayano, and H. Akagi, "Measurement and Reduction of EMI Radiated by a PWM Inverter-Fed AC Motor Drive System", *IEEE Transactions on Industry Applications*, vol. 33, Issue: 4, pp. 1019-1026, 1997.
33. H. Chung, S.Y.R. Hui, and K.K. Tse, "Reduction of EMI emission from power converter using soft-switching techniques", *IEE Electronics Letters*, vol. 32, Issue: 11, pp. 977-979, 1996.
34. J.H.B. Deane, and D.C. Hamill, "Improvement of power supply EMC by chaos", *IEE Electronics Letters*, 1996.
35. A.C. Wang, and S.R. Sanders, "Programmed pulsewidth modulated waveforms for electromagnetic interference mitigation in dc-dc converters", *IEEE Transactions on Power Electronics*, vol. 8, Issue: 4, pp. 596-605, 1993.
36. S. Musumeci, A. Raciti, A. Testa, A. Galluzzo, and M. Melito, "A new adaptive driving technique for high current gate controlled devices", *Applied Power Electronics Conference and Exposition*, vol.1, pp. 480 – 486, 1994.
37. S. Park. and T.M. Jahns, "Flexible dv/dt and di/dt control method for insulated gate power switches", *IEEE Transactions on Industry Applications*, vol. 39, Issue. 3, pp. 657 – 664, 2003.
38. G.L. Skibinski, R.J. Kerkman, and D. Schlegel, "EMI Emissions of Modern PWM AC Drives", *IEEE Industry Applications Magazine*, vol. 5, Issue: 6, pp. 47-81, 1999.
39. L. Tihanyi, *Electromagnetic Compatibility in Power Electronics*, IEEE Press, New Jersey, 1995.
40. R. Thomas, F. Li, and C. Garrett, "Prediction of radiated EMI from high frequency power converters", *Power Electronics and Variable Speed Drives*, pp. 80-85, 2000.
41. R. Sachdeva, and E.P. Nowicki, "A novel gate driver circuit for snubberless, low-noise operation of high-power IGBT", *Proceedings of the IEEE Canadian Conference on Electrical and Computer Engineering*, pp. 212-217, 2002.
42. X. Pei, K. Zhang, Y. Kang, and J. Chen, "Analytical estimation of common mode conducted EMI in PWM inverter", *IEEE Industry Application Society Conference*, vol. 4, pp. 2651 – 2656, 2004.